Estimating the relative phase-difference in EEG using the matched reassigned cross-spectrogram

Maria Åkesson

27th September 2021

Abstract

In brain connectivity research the relative phase between two EEG oscillations is particularly relevant, as it could provide information about the conduction delay between two regions. However, due to EEG signals containing large amounts of noise and spurious connections, the relative phase is seldom estimated. The aim of this thesis is to explore the possibilities of estimating relative phase using an algorithm based of the scaled reassigned spectrogram (ScRe-Spec) and the matched phase reassignment (MPR). Through simulations it is shown that both the Rényi entropy and the time-frequency concentration are suitable methods for evaluating the reassigned spectrograms. The algorithm is shown to give more correct estimations in comparison to other relative-phase estimation methods when the signal to noise ratio is low. Lastly, when tested on two real EEG-data examples, the algorithm shows promising results.

Populärvetenskaplig sammanfattning

Ny metod för att mäta fas-skillnader i hjärnsignaler

Bättre och mer robusta metoder för att mäta fas-skillnader mellan elektriska signaler i hjärnan behövs för att få bättre insikt i hur olika delar av hjärnan kommunicerar. I detta arbete undersöks en ny metod kallad *relokaliserat kors-spektrogram*. Denna metod visar sig vara mer exakt än två konventionella metoder under vissa förutsättningar.

Metoden introducerades först 2020 och går ut på att representera en sökt signal i både tid och frekvens, till skillnad från vanliga metoder som estimerar fas. På detta vis blir det lättare att urskilja den sökta signalen från störningar. Dessutom kan metoden representera signaler med mycket hög upplösning då dessa är i fas. Genom att förskjuta en signal i tid tills hög upplösning uppnås kan man estimera fas-skillnaden mellan signalerna.

Då signaler inspelade med elektroencefalografi (EEG), den vanligaste tekniken för att avläsa elektriska signaler i hjärnan, oftast domineras av störningar krävs det robusta metoder för att utläsa signalerna. Lyckligtvis var det just i signaler med mycket brus som den nya metoden klarade sig bättre än andra.

Det finns många fördelar med att använda sig av EEG för att avläsa hjärnsignaler, såsom att tekniken är billig och mobil, men framförallt är den inte invasiv. Detta gör tekniken attraktiv inom både sjukvård och forskning. Då fas-skillnaden mellan EEG-signaler kan ge mycket information om hur olika områden i hjärnan kommunicerar, skulle den nya metoden kunna bidra med kunskapsutveckling inom området. Eventuella variationer av den här typen av kommunikation i hjärnan kan vara relaterade till flera neurofysiologiska sjukdomar, såsom schizofreni, Parkinsons och Huntingtons sjukdom, men även autism och dyslexi. Det finns dessutom ett stort intresse inom psykologin att ta reda på var specifika minnen uppkommer i hjärnan, vilket kräver bättre och mer robusta metoder med hög upplösning för att analysera EEG. Detta skulle den nya metoden kunna uppfylla.

Den främsta nackdelen med den nya metoden är att den endast fungerar på korta signaler av en viss form. För att metoden ska kunna användas effektivt bör också viss information om signalen vara känd på förhand. Sammanfattningsvis har metoden goda förutsättningar för att kunna estimera fas-skillnader i EEG.

Acknowledgements

I am very thankful for having Maria Sandsten, Professor in Mathematical Statistics at Lund Univesity, as my supervisor during this project. Not only did she introduce me to the interesting topics of this thesis, but has also with patience and interest spent many hours discussing my thesis with me.

Furthermore, I would like to thank Mikael Johansson, Professor in Psychology at Lund University, for sharing the real data used in this thesis, and providing some insightful comments about how to start working with it.

I am very grateful to Stefan, who let me borrow his server to run simulations on when my own computer kept failing me.

Lastly, I would like to express my appreciation for my family and my partner, whom have given me much encouragement during the entirety of my time at university.

List of abbreviations

EEG - Electroencephalography

STFT - Short-term Fourier transform

ScRe-Spec - Scaled reassigned spectrogram

MPR - Matched phase reassigned cross-spectrogram

TF - Time-frequency

RE - Rényi entropy

TFC - Time-frequency concentration

GI - Gini index

ERP - Event related potential

PLV - Phase locking value

PLI - Phase lag index

LTI - Linear time-invariant

FIR - Finite impulse response

IIR - Infinite impulse response

SNR - Signal-to-noise ratio

MSE - Mean square error

ERO - Event related oscillation

Contents

1 Introduction

Electroencephalography (EEG) is a monitoring method of the electrical activity present on the scalp, and can give insight of the neurological processes underneath. It is extensively used for diagnosing epilepsy, sleep disorders and brain death [1] and is also commonly used in research of various neurological disorders and conditions. EEG can furthermore be used for Brain Computer Interface (BCI) applications, and has the great advantage of being non-invasive, as well as affordable and practical in real applications [2].

In recent years, much research has been dedicated to *brain connectivity* as it is believed to play an important role in neural communication between different areas of the brain. Brain connectivity is therefore essential in both basic and applied neurobiological research. Furthermore, several neurological disorders and variations are believed to be connected to variations in brain connectivity, such as Parkinson's and Huntington's disease, schizophrenia, autism and dyslexia [3].

The relative phase between different EEG oscillations is particularly relevant in EEG brain connectivity measurements. Phase-synchronization measurements aims to measure phase consistency between oscillations, which indicates connectivity. In these measurements, the instantaneous relative phase is a key component and is estimated using the Hilbert transform. In other connectivity measurements, such as cross-correlation, the relative phase influence the measurements indirectly. Although the relative phase is a central characteristic in brain connectivity, and could provide information about the conduction delay between two regions [4], it is seldom estimated directly. The reason for this could be a lack of robust estimation methods that can withstand the large amounts of noise present in EEG. This thesis will attempt to close this gap by exploring the possibilities of an alternative method for estimating the relative phase in EEG.

In Sandsten et al. [5], the matched-phase reassignment (MPR), a novel estimation method of the relative phase is introduced. The method aims to reassign the energy of a cross-spectrogram between two transient signals with known equal envelopes. As optimal time-frequency resolution of the reassigned cross-spectrogram only is achieved when the signals are in phase, a time-shift corresponding to the relative phase can be found. A related method called the scaled reassigned spectrogram (ScRe-Spec) have been used to estimate signal parameters of transient Gaussian signals [6] [7].

In this thesis, a two-step algorithm to estimate relative phase will be implemented, combining the ScRe-Spec with the MPR method. Through simulations, the thesis aims to improve the understanding of and further investigate the ScRe-Spec and the MPR. The two-step algorithm will then be used on two real data examples in order to explore its possibilities for EEG applications. The thesis aims to answer the following questions:

- Which time-frequency concentration measurement is best suited for evaluation of the reassigned cross-/spectrograms in the two-step algorithm - the Rényi entropy (RE), the time-frequency concentration (TFC) or the Gini index (GI)?

- How accurate is relative phase estimation using the two-step reassignment method in comparison to other established methods?

- Is it possible to estimate relative phase between signals in EEG using the implemented two-step reassignment method?

2 Theory

This chapter aims to briefly introduce the reader to the subjects relevant to this thesis. In Section 2.1 the spectrogram and variants of the reassigned spectrogram will be presented. The concentration measurements used to evaluate the reassignments in this project are listed in Section 2.2. A brief introduction of EEG and filters are found in Section 2.3 and 2.4 respectively.

2.1 Time-frequency analysis of transient signals

Signals of very short duration in comparison to a entire measurement are often referred to as transients or transient signals. In this thesis project, we will define transient signals to be of the following form

$$x(t) = a(t - t_0)e^{-j\omega_0 t}, \tag{2.1}$$

where t_0 is the centre time, ω_0 is the frequency and a is the envelope. In Figure 2.1(a) and (b), two examples of transient signals are plotted.
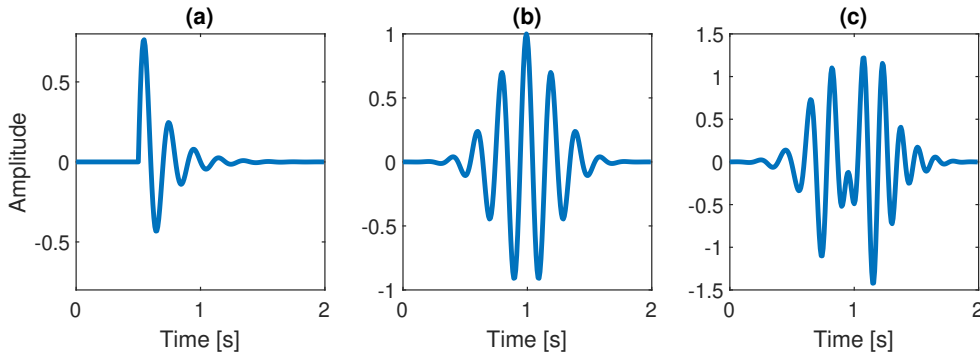

Figure 2.1: Examples of transient constant frequency signals. The sampling frequency is $f_s = 128$ Hz. In (a), the envelope is given by a decaying exponential function (with zero for $t < 0$) with $t_0 = 0.5$ s and $f_0 = 5$ Hz. In (b), the envelop of the signal is Gaussian with $t_0 = 1$ s, $f_0 = 5$ Hz and $\sigma = 30$. The plot in (c) illustrates two transients with equal Gaussian envelopes, where $\sigma_1 = \sigma_2 = 30$ but different centre times and frequencies. For the first signal $t_{01} = 0.90$ s and $f_{01} = 5$ Hz, and for the second signal $t_{02} = 1.1$ s and $f_{02} = 7$ Hz.

In (b) the envelope is given by a Gaussian function, such that $a(t) = g(t)$, where

$$g(t) = \exp\left(\frac{-t^2}{2\sigma^2}\right). \tag{2.2}$$

The scaling parameter σ regulates the length of the signal. The length of such a signal we define as the length in which 99% of the energy resides, that is

$$\frac{1}{\sigma\sqrt{\pi}} \int_{-L/2}^{L/2} g(t)^2 \mathrm{d}t = 0.99, \tag{2.3}$$

3

where $\sigma\sqrt{\pi} = \int_{-\infty}^{\infty} g(t)^2 \mathrm{d}t$ is the total energy of a Gaussian signal. Solving the equation above, the signal length is then given by

$$L = 2\sigma \operatorname{erf}^{-1}(0.99), \tag{2.4}$$

where erf^{-1} is the inverse error function. In Figure 2.1(c), two transient Gaussian signals of equal length and different frequencies are seen. These will serve as examples for the time-frequency representation methods in the following sections.

2.1.1 The spectrogram

In order to gain better understanding of the time and frequency content in a non-stationary or transient signal, the signal is often represented in the time-frequency domain. The most common time-frequency representation is the spectrogram, which is given by

$$S_x^h(t, \omega) = |F_x^h(t, \omega)|^2, \tag{2.5}$$

where

$$F_x^h(t, \omega) = \int x(\tau) h^*(\tau - t) e^{-j\omega\tau} \mathrm{d}\tau. \tag{2.6}$$

is the short-time Fourier transform (STFT) with window function h of time-series x. The window function h is chosen such that it is centred around t, which makes the STFT a local measurement of the frequency content in x around t. The shape of the window-function affects the resolution in different ways, where some windows might increase the possibility to detect low amplitude signals and others may reduce them [8]. One commonly used window function is the unit energy Gaussian function given by

$$h_\lambda(t) = \frac{1}{\pi^{1/4}\sqrt{\lambda}} \exp\left(\frac{-t^2}{2\lambda^2}\right) \tag{2.7}$$

where λ is a parameter which regulates the length of the window. Due to the uncertainty principle, the choice of λ affects the time-frequency resolution of the spectrogram [8]. When the window is long, more frequency content of the signal is available and similar frequencies are more easily separated. However, this comes at the expense of a more smeared out signal in time. This is illustrated in Figure 2.2, where the spectrogram of the signals in Figure 2.1(c) is illustrated for different choices of λ.

Several other methods have been suggested to achieve increased resolution in time-frequency representations, for example the Wigner distribution and ambiguity kernels. Another method which has gained much attention in recent years is the reassigned spectrogram.

2.1.2 The reassigned spectrogram & the scaled reassigned spectrogram (ScRe-Spec)

The main idea of the reassigned spectrogram is, as the name suggests, to reassign the energy of the spectrogram to more localised points. How the energy is re-distributed is determined by the reassignment vectors $\hat{t}(t, \omega)$ and $\hat{\omega}(t, \omega)$. According to these vectors,
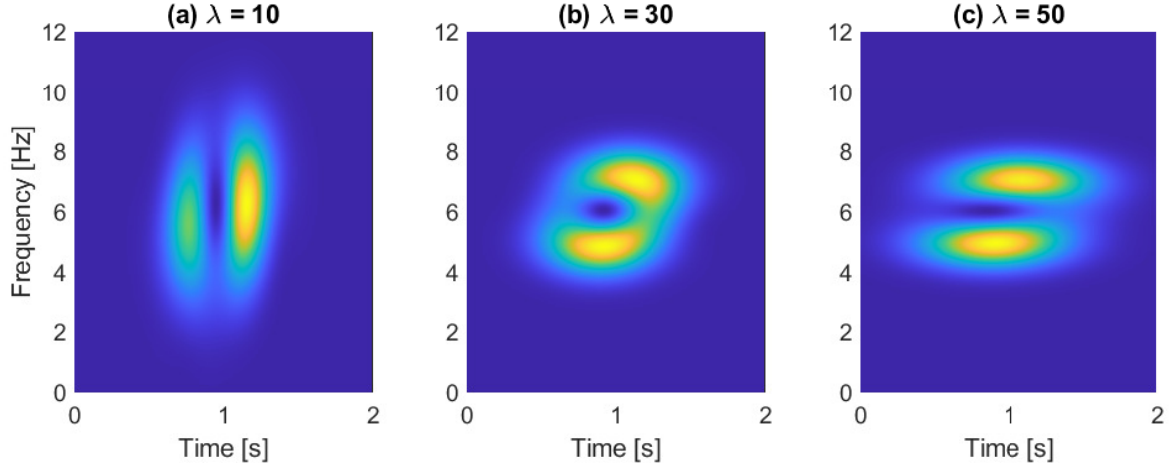
Figure 2.2: Spectrogram of signals in Figure 2.1(c), using Gaussian windows with
different parameters λ. When the window is short in (a), the signals are well
separated in time but smeared out in frequency. Using a long window as in
(c), the signals are well separated in frequency but smeared out in time.

the energy in (t, ω) is moved to the new point $(\hat{t}(t, \omega), \hat{\omega}(t, \omega))$. Optimal reassignment
is achieved when all energy is reassigned to the centre time t_0 and frequency ω_0 of the
signal, such that $(\hat{t}(t, \omega), \hat{\omega}(t, \omega)) = (t_0, \omega_0)$.

The reassigned spectrogram is given by [9]

$$RS_x^h(t, \omega) = \int \int S_x^h(s, \xi) \delta(t - \hat{t}_x(s, \xi), \omega - \hat{\omega}_x(s, \xi)) \mathrm{d}s \mathrm{d}\xi \qquad (2.8)$$

where S_x^h is the spectrogram of signal x using some window function h, and δ is the
two-dimensional Dirac-delta function, such that

$$\int \int f(x, y) \delta(x - x_0, y - y_0) \mathrm{d}x \mathrm{d}y = f(x_0, y_0). \qquad (2.9)$$

The reassignment vectors are given by

$$\hat{t}(t, \omega) = t + c_t \Re \left(\frac{F_x^{th}(t, \omega)}{F_x^h(t, \omega)} \right) \qquad (2.10)$$

$$\hat{\omega}(t, \omega) = \omega - c_\omega \Im \left(\frac{F_x^{\mathrm{d}h/\mathrm{d}t}(t, \omega)}{F_x^h(t, \omega)} \right), \qquad (2.11)$$

where F_x^{th} and $F_x^{\mathrm{d}h/\mathrm{d}t}$ are the STFT of x using window function $t \cdot h(t)$ and $\mathrm{d}h/\mathrm{d}t$
respectively. If the constants are set to $c_t = c_\omega = 1$, the original (or normal) reassign-
ment is archived.

The reassignment vectors in Equations 2.10 and 2.11 can be further simplified if certain
assumptions about the signal and window function are made. If x is given by a tran-
sient signal defined as in Equation 2.1, it has been shown that optimal reassignment
is achieved when $h(t) = a(-t)$, and $c_t = c_\omega = 2$ [10]. In Sandsten and Brynolfsson [6]
and Brynolfsson and Sandsten [7], they derive the reassignment vectors for the scaled
reassigned spectrogram (ScRe-Spec). If x is assumed to be a transient signal with a

5

Gaussian-envelope with scaling parameter σ, and the window function is given by the unit-energy Gaussian with parameter λ in Equation 2.7, the reassignment vectors are simplified to [6] [7]

$$\hat{t}(t,\omega) = t - c_t \frac{\lambda^2}{\lambda^2 + \sigma^2}(t - t_0) \tag{2.12}$$

$$\hat{\omega}(t,\omega) = \omega - c_\omega \frac{\sigma^2}{\lambda^2 + \sigma^2}(\omega - \omega_0). \tag{2.13}$$

Optimal reassignment is achieved when the constant scaling factors in Equation 2.12 and 2.13 are set to

$$c_t = \frac{\lambda^2 + \sigma^2}{\lambda^2} \tag{2.14}$$

$$c_\omega = \frac{\lambda^2 + \sigma^2}{\sigma^2}. \tag{2.15}$$

Optimal reassignment can therefore be achieved for any λ if the scaling parameter, σ, is known. This is of course rarely the case. However, the scaling parameter σ can be estimated from a set of predefined candidates σ_i by choosing the candidate which gives the most concentrated ScRe-Spec. In Figure 2.3, scaled reassigned spectrograms for different candidates are shown. It is seen that optimal reassignment indeed occurs when $\sigma_i = \sigma$ in (b).
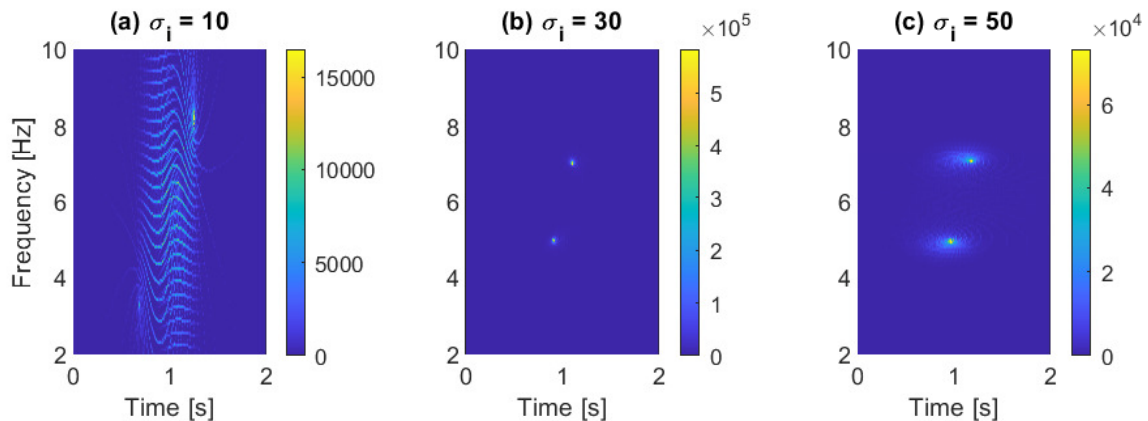

Figure 2.3: ScRe-Spec of signals in Figure 2.1(c). In (a), (b) and (c), different candidate scaling parameters σ_i are used in the reassignment vectors in Equation 2.14 and 2.15. The Gaussian window parameter is set to $\lambda = 40$, and the true scaling is $\sigma = 30$.

A summary of how the scaling parameter σ can be estimated using this method is shown below. In Brynolfsson and Sandsten [7], a more complex version of this algorithm is used, including several iterations with zoomed in directories of candidate scaling parameters σ_i, and a non-linear least-square minimisation step to fine-tune the

parameters.

Algorithm 1: Estimation of σ using the ScRe-Spec

Define vector of candidate scaling parameters σ_i.
Calculate $S_x^h = |F_x^h|^2$, F_x^{th} and $F_x^{\mathrm{d}h/\mathrm{d}t}$ using window h_λ in Equation 2.7.
for *each σ_i* **do**

   Set $c_t = \frac{\lambda^2 + \sigma_i^2}{\lambda^2}$

   Set $c_\omega = \frac{\lambda^2 + \sigma_i^2}{\sigma_i^2}$

   Calculate the ScRe-Spec according to Equation 2.8.
   Calculate the concentration of the ScRe-Spec.

end
Choose the candidate σ_i which gives optimal concentration.

The concentration of the ScRe-Spec is calculated using one of the concentration measurements presented in Section 2.2.

2.1.3 The matched phase reassigned cross-spectrogram (MPR)

In Sandsten et al. [5] the theory of matched reassigned spectrograms was extended to cross-spectrograms. The cross-spectrogram between two signals y_1 and y_2 is given by

$$S_{y_1,y_2}^h(t,\omega) = F_{y_1}^h(t,\omega)(F_{y_1}^h(t,\omega))^*, \qquad (2.16)$$

where $F_{y_n}^h$ once again is the STFT with some window function h. The general reassigned cross-spectrogram is similar to before given by

$$RS_{y_1,y_2}^h(t,\omega) = \int\int |S_{y_1,y_2}^h(s,\xi)|\delta(t-\hat{t}_{y_1,y_2}(s,\xi))\delta(\omega-\hat{\omega}_{y_1,y_2}(s,\xi))\mathrm{d}s\mathrm{d}\xi, \qquad (2.17)$$

with the following reassignment vectors

$$\hat{t}_{y_1,y_2}(t,\omega) = t + c_t\Re\left(\frac{F_{y_1}^{th}}{F_{y_2}^h} + \frac{F_{y_2}^{th}}{F_{y_1}^h}\right) \qquad (2.18)$$

$$\hat{\omega}_{y_1,y_2}(t,\omega) = \omega - c_\omega\Im\left(\frac{F_{y_1}^{\mathrm{d}h/\mathrm{d}t}}{F_{y_2}^h} + \frac{F_{y_2}^{\mathrm{d}h/\mathrm{d}t}}{F_{y_1}^h}\right). \qquad (2.19)$$

If the two signals are further assumed to be given by

$$y_n(t) = A_n x(t)\mathrm{e}^{-j\phi_n}, \quad n = 1, 2, \qquad (2.20)$$

where $x(t)$ is a transient signal defined in Equation 2.1, and the window function is assumed to match the signal envelope $h(t) = a(-t)$, the reassignment vectors can be simplified to

$$\hat{t}_{y_1,y_2}(t,\omega) = t - c_t\frac{1}{2}\frac{A_1^2 + A_2^2}{A_1 A_2}\cos(\phi_2 - \phi_1)(t - t_0) \qquad (2.21)$$

$$\hat{\omega}_{y_1,y_2}(t,\omega) = \omega - c_\omega\frac{1}{2}\frac{A_1^2 + A_2^2}{A_1 A_2}\cos(\phi_2 - \phi_1)(\omega - \omega_0), \qquad (2.22)$$

where A_n is the amplitude and ϕ_n is the phase of the n:th signal. From the expressions, we see that optimal reassignment, i.e. $\hat{t}_{y_1,y_2}(t,\omega) = t_0$ and $\hat{\omega}_{y_1,y_2}(t,\omega) = \omega_0$, occurs when $c_t = c_\omega = 2A_1A_2/(A_1^2 + A_2^2)$ and $\phi_2 - \phi_1 = 0$.

Because of this, the method is suggested to be used for estimation of relative phase $\Delta\phi = \phi_2 - \phi_1$ between two signals. As a phase difference corresponds to a time-shift according to

$$\Delta t = \frac{\Delta\phi}{2\pi}T, \tag{2.23}$$

where T is the period, the relative phase can be estimated by applying time-shifts to the second signal and find which time-shift gives optimal concentration of the reassigned cross-spectrogram.

As the signals and the spectrogram in practice are discrete in time and frequency, the minimal time-shift that can be applied is the sample time, or $1/f_s$, where f_s is the sampling frequency. For the rest of this report, the time-shift will be expressed in number of samples, denoted k and called time-lag. The estimated time-lag will be denoted $\hat{k}$ and the true time-lag is denoted $k_0 = \frac{\Delta\phi}{2\pi}T\frac{1}{f_s}$.

A summary of the relative phase-estimation procedure described in Sandsten et al. [5] is presented below.

Algorithm 2: Estimation of $\Delta\phi$ using the MPR

Define vector of candidate time lags k_i.

for *each k_i* **do**

    Apply the time lag to the second signal, such that $y_2'(t) = y_2(t + k_i)$.
    The first signal is still $y_1'(t) = y_1(t)$.
    Calculate $F_{y_n'}^h$, $F_{y_n'}^{th}$, $F_{y_n'}^{dh/dt}$ using window h in Equation 2.7.
    Estimate amplitudes $\hat{A}_1$, $\hat{A}_2$.
    Set $c_t = c_\omega = 2\frac{\hat{A}_1\hat{A}_2}{\hat{A}_1^2 + \hat{A}_2^2}$.
    Calculate the MPR according to Equation 2.17.
    Calculate the concentration of the spectrogram.

end

Choose the candidate k_i which gives optimal concentration.

In the paper, the amplitudes were estimated as the maximum amplitudes of the signals. Next, some possible concentration measurements will be presented.

2.2   Measurements of time-frequency concentration

Several different concentration measurements have been suggested in order to evaluate the performance of TF-representations [11]. As previously mentioned, the TF-representations are in practice discrete. The evaluation methods below will therefore be presented over discrete time n and frequency m. Usually the spectrograms are calculated using fast Fourier transform (FFT), which computes N_{FFT} spectrogram values for frequencies between 0 Hz and f_s Hz, excluding f_s.

Rényi entropy (RE)

The Rényi entropy is currently the most popular measurement for evaluating the reassigned spectrogram [5, 6, 7, 10], and is the one used in the two algorithms above. For any discrete TF-representation, $S(n,m)$, the Rényi entropy over a chosen region is given by

$$RE = \frac{1}{1-\alpha} \log_2 \sum_{n_1}^{n_2} \sum_{m_1}^{m_2} \left(\frac{S(n,m)}{\sum_{n_1}^{n_2} \sum_{m_1}^{m_2} S(n,m)} \right)^\alpha \qquad (2.24)$$

where α, due to stability advantages, usually is set to 3 [12]. The discrete region $n \in [n_1, n_2]$ and $m \in [m_1, m_2]$ corresponds to some region in time-frequency, $t \in [t_1, t_2]$ and $\omega \in [\omega_1, \omega_2]$. In the equation above, $S(n,m)$ is normalised by its energy in the chosen region. Another option is to normalise $S(n,m)$ by its volume. Then, the volume normalised Rényi entropy is given by

$$VRE = \frac{1}{1-\alpha} \log_2 \sum_{n_1}^{n_2} \sum_{m_1}^{m_2} \left(\frac{S(n,m)}{\sum_{n_1}^{n_2} \sum_{m_1}^{m_2} |S(n,m)|} \right)^\alpha. \qquad (2.25)$$

For both RE and VRE, more concentrated TF-representations result in smaller measurement values. As the reassigned spectrogram always is real-valued and non-negative, the two measurements will yield the same results.

Time-frequency concentration (TFC)

Similar to kurtosis, the time-frequency concentration (TFC) measures the "sharpness" or "peakness" of a TF-representation. The TFC is given by

$$TFC = \frac{\sum_{n_1}^{n_2} \sum_{m_1}^{m_2} S^4(n,m)}{\left(\sum_{n_1}^{n_2} \sum_{m_1}^{m_2} S^2(n,m) \right)^2}, \qquad (2.26)$$

where more concentrated TF-representations result in a higher TFC-value.

Gini Index (GI)

The Gini Index (GI) was first introduced in economics as a measurement of inequality in wealth distribution. As GI, in more general terms, measures the sparsity in a distribution, it has been shown to be a suitable measurement in other fields as well, for example in signal processing [13]. To calculate the GI for TF-distributions, all values of $S(n,m)$ over the chosen region, $n \in [n_1, n_2]$, $m \in [m_1, m_2]$, are first organised into a sorted vector $s(1) \leq s(2) \leq ... \leq s(N)$. Then, the GI is given by

$$GI = 1 - 2 \sum_{l=1}^{N} \frac{s(l)}{||x||_l} \frac{N - l + 0.5}{N}, \qquad (2.27)$$

where $||x||_1 = \sum_{l=1}^{N} |s(l)|$. More concentrated TF-representations are more sparse and have more unequal distribution of power, and therefore give higher values of GI.

2.3 Connectivity in EEG

2.3.1 The cerebral cortex & EEG signals

The cerebral cortex is the out-most layer of the brain, about 2 to 3 mm thick. Different regions of the cortex are primarily responsible for different functions such as speech, voluntary movement and different senses as seen in Figure 2.4a. The whole cortex consists of roughly 10 billion neurons, which collectively generate a measurable electric field.

Electroencephalography (EEG) is one monitoring method, where electrical activity present on the scalp is measured by electrodes. The electrodes are usually placed according to the standardised 10-20 system. This system involves placement of electrodes on the pre-frontal (Fp), fronal (F), temporal (T), parietal (P), occipital (O), and central (C) lobe. In order to increase resolution, a new 10-20 system has been introduced with more electrodes. The electrode placement of this system is seen in Figure 2.4b.

EEG signals often exhibit oscillatory behaviour and are in many cases well modelled as short-term stationary processes. Certain frequency bands are especially common and their origin have been subject for investigation for as long as EEG has existed. The *delta rhythm*, < 4 Hz, is of large amplitude and is prominent during deep sleep. The *theta rhythm*, $4 - 7$ Hz, occurs during drowsiness, the *alpha rhythm*, $8 - 13$ Hz, is most prominent in relaxed states in the occipital region when the subjects eyes are closed, and the *beta rhythm*, $14 - 30$ Hz, is of low amplitude in the fronal and central regions of the scalp mainly during certain stages of sleep. The highest frequency band is the *gamma rhythm*, > 30 Hz, and can be found during active information processing [1, p. 34]. In memory research, alpha and beta rhythms appears to be related to semantic encoding [1], whereas theta and gamma rhythms are activated during non-semantic encoding [14].

Event related potentials (ERP) are measurable electrical responses to external stimuli. These are often well-modelled as deterministic [1, p.194-195], and are characterised by their very short duration and low amplitude compared to the stochastic oscillations described previously. In settings where ERPs are of interest, the stochastic oscillations are therefore often considered as noise, even though they are of neurological origin. Also of neurological origin is the 1/f-noise, which is characterised by a power spectrum that decays as $1/f$ [15].

2.3.2 Connectivity measurements

The brain is made up by a network of neurons. The connections between neural masses can be either *anatomical*, which describes physical connections, or *functional*, which refers to simultaneous activation of similar patterns in different regions of the brain. An

---

[1]Semantic processing, in a psychological context, is the processing happening after we hear a word, making us put it in a context which leads to deeper encoding of its meaning. Non-semantic, or shallow, encoding is easier to forget.
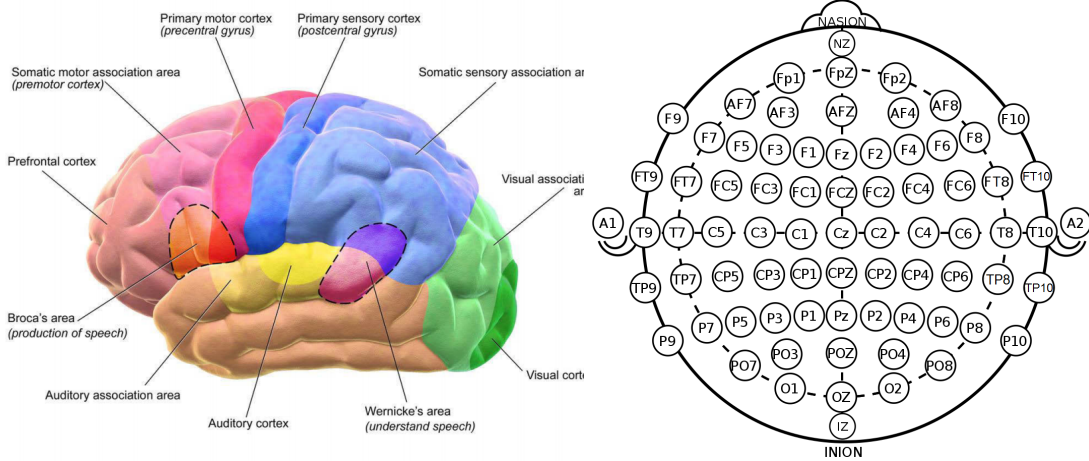
(a) Illustration of the cerebral cortex and the placement of areas primarily related to certain neurological functions. [16]

(b) Image of the electrode placement in the new 10-20 system [17].

.

Figure 2.4

extension of the latter is *effective connectivity*, which also intends to measure a causal relationship between neural masses [18]. As functional and effective connectivity are believed to play an important role in neural communication, much research is dedicated to the topic.

Many functional and effective connectivity measurements aim to measure, either directly or indirectly, the consistency between phases of EEG oscillations. Some of these are presented below.

Hilbert transform

The instantaneous relative phase $\Delta\phi(t)$ between two time-series s_1 and s_2 can be estimated from the complex-valued analytic series z_1 and z_2. These are given by [19]

$$z_i(t) = s_i(t) + j\text{HT}(s_i(t)), \tag{2.28}$$

where HT is the Hilbert transform. The relative phase between two such signals are given by

$$\Delta\phi(t) = \arg\left(\frac{z_1(t)z_2^*(t)}{|z_1(t)||z_2(t)|}\right), \tag{2.29}$$

where z_2^* is the complex conjugate of z_2.

Although the Hilbert transform is sometimes used to estimate relative phase directly as a measurement of effective connectivity [20], it is perhaps more often found for calculating the phase-locking value (PLV) or the phase lag index (PLI) presented below.

In Kovach [21] some concerns about these measurements are presented. As the computation of the analytic signal, directly or indirectly, involves a non-linear operation that introduces broad spectral leakage, these measurements may sometimes be difficult to interpret.

Phase-Locking Value (PLV)

The PLV is commonly used for measuring phase synchronization, which is a measurement of functional connectivity. For two channels, the PLV is given by [19]

$$PLV = |\frac{1}{T}\sum_{t=0}^{T-1} e^{j\Delta\phi(t)}|, \tag{2.30}$$

where T is the number of samples and $\Delta\phi(t)$ is the relative phase given by the Hilbert transform in Equation 2.29. The expression should be interpreted as a summation of vectors of length one in the complex plane. If the vectors are all in the same direction, and thus have equal relative phases, the resulting PLV is one. If the relative phases differ and the vectors are not in the same direction, the resulting PLV is less than one, with a minimal value of zero. The PLV is thus a measure of consistency of the relative phases $\Delta\phi(t)$.

Phase Lag Index (PLI)

Similar to the PLV, the PLI is a phase synchronization measurement used to measure functional connectivity, and is given by [19]

$$PLI = |\frac{1}{T}\sum_{t=0}^{T-1} \text{sign}(j\Delta\phi(t))|. \tag{2.31}$$

Due to the sign-function in the expression, the PLI will be insensitive to relative phases of 0. This is can sometimes be an advantage compared to the PLV due to reasons that will be described on the next page.

Pearson's linear correlation coefficient (CORR)

Pearson's linear correlation coefficient (CORR) is sometimes used to measure functional connectivity [22]. It is given by

$$CORR = \frac{\sum_{t=t_1}^{t_2}(y_1(t) - \overline{y}_1)\sum_{t=t_1}^{t_2}(y_2(t) - \overline{y}_2)}{\sqrt{\sum_{t=t_1}^{t_2}(y_1(t) - \overline{y}_1)^2}\sqrt{\sum_{t=t_1}^{t_2}(y_2(t) - \overline{y}_2)^2}}, \tag{2.32}$$

where it has been limited to time samples between t_1 and t_2. The mean value during this time interval is denoted $\overline{y_i}$.

Other measurements

In addition to the phase synchronization measurements PLV and PLI, and functional connectivity measurement CORR, other measurements have been suggested, such as spectral coherence and Granger causality. Measurements of effective connectivity other than the Hilbert transform are Granger causality, transfer entropy and correlation [20].

2.3.3 Problem with source leakage

In all these measurements, one needs to be cautious of source leakage [18]. When electrical activity originating from two separate sources is measured by electrodes on the scalp, electrical activity from one source can 'leak out' and mix with the electrical activity from the other source. As the same activity is measured in both electrodes, they falsely seem to be phase synchronized. The relative phase between the electrode measurements will be zero, as the source leakage is instantaneous. Some phase-synchronization measurements are especially equipped to tackle such spurious connections, such as PLI, but are equally insensitive to true zero-lag connections. Another way to reduce the influence of source leakage is by first applying a spatial filter, such as the surface Laplacian [23].

2.4 Brief overview of filters

Given a discrete time-varying input signal $x(n)$, the output signal from a linear time-invariant (LTI) filter is given by the following convolution

$$y(n) = (h * x)(n) = \sum_{k=-\infty}^{\infty} h(k)x(n-k), \tag{2.33}$$

where h now is the filter impulse response. When the input is an impulse, that is, a Dirac delta function δ, the output is simply given by the impulse response. The convolution in Equation 2.33 is equivalent to multiplication in frequency domain, such that

$$Y(\omega) = H(\omega)X(\omega), \tag{2.34}$$

where H is called the transfer function.

LTI filters are often divided into two categories, finite impulse response (FIR) filters and infinite impulse response (IIR) filters [24]. Causal FIR filters can be further expressed as

$$y(n) = \sum_{k=0}^{M-1} b_k x(n-k), \tag{2.35}$$

where b_k is the k:th filter coefficient and M is the number of coefficients. As the output only depends on the input values, the impulse response is finite. These filters are therefore always stable and are easy to implement. Also, if the impulse response is symmetric, the FIR filter will have linear phase response. This means that no phase distortion of the signal will occur.

Causal IIR filters can be written as

$$y(n) = -\sum_{k=1}^{N} a_k y(n-k) + \sum_{k=0}^{M-1} b_k x(n-k), \tag{2.36}$$

where the output depends on both input values and previous output values. The recursive behaviour of the filter makes the input response infinite. These filters are

very computationally efficient as they typically require very few filter coefficients in comparison to FIR filters. They will however have a non-linear phase response such that the original phases of the input-signal will be distorted.

In offline filtering settings, causal IIR filters can be filtered both forward and backward in time to achieve zero-phase filtering. The entire filtering operation is non-causal and is called forward-backward filtering [25].

3 The two-step algorithm

The main goal of the algorithm is to estimate a time-lag $\hat{k}$ corresponding to the relative phase $\Delta\phi$ between two transient signals y_1 and y_2. The MPR procedure in Algorithm 2 assumes that the envelope $a(t)$ of the signals is known and uses the matched window, $h(t) = a(-t)$, in the STFT. In settings where the signal-to-noise ratio (SNR) is low, such as in EEG, this assumption may be difficult to fulfil. By assuming the signals to have Gaussian envelopes, they at least can be allowed to be of unknown length. Then, the ScRe-Spec in Algorithm 1 can be used to first estimate the scaling parameter σ, which determines the signal length, and after that the MPR can be used to estimate the relative phase using a matched Gaussian window.

To put simply, the two-step algorithm is constructed as follows:

1. Estimate the scaling parameter σ of both y_1 and y_2 using the ScRe-Spec in Algorithm 1. Then, take the average of these estimations as the final estimation $\hat{\sigma}$.

2. Estimate the time-lag $\hat{k}$ using the MPR in Algorithm 2, where the window is given by a unit energy Gaussian function with scaling parameter $\hat{\sigma}$.

A more detailed description of the procedure is presented in Algorithm 3 on the next page. In the algorithm, the scaling parameter can be estimated iteratively if $J > 1$, such that the ScRe-Spec is initialized with some λ, and then updated with the previous estimation $\hat{\sigma}$. The signal amplitudes can be estimated from the square root of the maximum amplitude of the spectrogram inside the defined region $t \in [t_1, t_2]$ $f \in [f_1, f_2]$. In addition to the scaling parameter and time-lag estimations, the centre time t_0 and frequency f_0 can be estimated from the maximum value of the MPR. In the next chapter, simulations will be made to determine the following:

- Whether the scaling of the window should be iteratively estimated, that is, whether J in Algorithm 3 should be one or more.

- Which TF-concentration measurement should be used.

In the beginning of the project, another algorithm for estimating $\hat{\sigma}$ and $\hat{k}$ under the same assumptions was constructed. A variant of the MPR was used and the TF-concentration was calculated over a grid of candidate scaling parameters and time-lags (σ_i, k_j). As this method was both slower and less robust than the two-step method, it was soon discarded. The MPR variant that was used in this algorithm is presented in Appendix A.1.

Algorithm 3: Two-step algorithm for estimation of time-lag k.

Define a vector of candidate scaling parameters σ_i.

Define a vector of candidate time-lags k_i.

Define a region, $t \in [t_1, t_2]$, $f \in [f_1, f_2]$, over which the TF concentration of the reassignments should be measured.

Set initial window function parameter λ_1.

for *j=1,...,J, or until convergence* **do**

> Calculate the ScRe-Spec of signal 1, y_1, using window function parameter λ_j for each σ_i. Choose the candidate σ_i which gives optimal concentration over the defined region as the estimate $\hat{\sigma_1}$.
>
> Calculate the ScRe-Spec of signal 2, y_2, using window function parameter λ_j for each σ_i. Choose the candidate σ_i which gives optimal concentration over the defined region as the estimate $\hat{\sigma_2}$.
>
> Set $\hat{\sigma} = \frac{\hat{\sigma_1} + \hat{\sigma_2}}{2}$.
>
> Update window function parameter $\lambda_{j+1} = \hat{\sigma}$.

end

for *each k_i* **do**

> Apply time delay to signal 2, such that $y'_2(k) = y_2(k + k_i)$.
>
> Signal 1 is still $y'_1(k) = y_1(k)$.
>
> Calculate $F^h_{y'_n}$, $F^{th}_{y'_n}$, $F^{dh/dt}_{y'_n}$ using a unit energy Gaussian window with scaling parameter $\hat{\sigma}$.
>
> Estimate amplitudes $\hat{A}_1$, $\hat{A}_2$.
>
> Set $c_t = c_\omega = 2\frac{\hat{A}_1 \hat{A}_2}{\hat{A}_1^2 + \hat{A}_2^2}$
>
> Calculate the reassignment vectors from Equation 2.12 and 2.13. Calculate the reassigned cross-spectrogram according to Equation 2.17.
>
> Calculate the TF-concentration of the reassigned cross-spectrogram over the defined region.

end

Choose the time-lag k_i which gives optimal concentration.
---

4 Simulations

4.1 Overview

Before the two-step algorithm was used on real EEG-data, the two parts were first tested on simulated data for two kinds of noise and different signal-to-noise ratios (SNR). Both white Gaussian noise and simulated EEG-noise was used. In all simulations, the sampling frequency was set to $f_s = 128$ Hz, and $M = 300$ trials were simulated for each SNR-level. The spectrograms were calculated using $N_{FFT} = 1024$ points in the FFT. The signal scaling parameters were always $\sigma = 50$ samples long, with $t_0 = 1.51$ s and $f_0 = 7$ Hz. The signal phases were generated as $\phi_1 \sim \mathcal{U}(-\pi, \pi)$, and $\phi_2 = \phi_1 + \Delta\phi$, where $\Delta\phi$ was varied between simulations. The simulated time-series were $N = 512$ samples long.

In Table 4.1, an overview of all simulations can be seen. After the SNR definition and EEG-noise model have been introduced, the simulations will be presented in greater detail in Sections 4.2 through 4.4.

4.1.1 Definition of signal-to-noise ratio (SNR)

The simulated time-series are given by

$$z_i(t) = y_i(t) + n_i(t), \quad i = 1, 2, \tag{4.1}$$

where $y_i(t)$ is the transient signal defined in Equation 2.20, and $n_i(t)$ is the noise in respective channel. The noise in each channel have identical spectral density, such that $R_n(\omega) = R_{n1}(\omega) = R_{n2}(\omega)$. The total noise power in each channel is calculated as

$$P_n = \frac{1}{2\pi} \int_{-\pi f_s}^{\pi f_s} R_n(\omega) \mathrm{d}\omega, \tag{4.2}$$

where f_s is the sampling frequency.

The SNR is then defined as

$$SNR = \log_{10} \left(\frac{\max\limits_t y_1(t)^2}{P_n} \right) \tag{4.3}$$

where $\max\limits_t y_1(t)^2$ is the maximum squared amplitude of signal 1. Instead of the squared amplitude, the transient signal energy is often used. This was however considered to be inconvenient as this definition would depend on the number of samples used. Moreover, the SNR definition i Equation 4.3 enables straight-forward comparisons between simulations where the amplitude of the second signal varies as the noise amplitude remains constant. As the amplitude of signal 2 decreases, the problem gets more difficult.

Simulation	Conc. meas.	Noise	$\Delta\phi$	A_1, A_2
Section 4.2. Estimation of signal scaling parameter σ using iterative, $J = 4$, or non-iterative, $J = 1$, ScRe-Spec with different concentration measurements.	All	White	$\mathcal{U}(-7\pi/8, 7\pi/8)$	1
		EEG	$\mathcal{U}(-7\pi/8, 7\pi/8)$	1
Section 4.3. Estimation of time lag k using MPR with different concentration measurements.	All	White	$\mathcal{U}(-7\pi/8, 7\pi/8)$	1
		EEG	0	1
		EEG	$\mathcal{U}(\pi/8, 7\pi/8)$	1
		EEG	$\mathcal{U}(-7\pi/8, 7\pi/8)$	1
Appendix A.2. Amplitude estimation.	RE	White	$\mathcal{U}(-7\pi/8, 7\pi/8)$	Varied
		EEG	$\mathcal{U}(-7\pi/8, 7\pi/8)$	Varied
Section 4.4.1. Disturbance signal at time $t_0 + \Delta t$ but equal frequency. Phases of disturbance signals are $\phi_{d1} = 5/8\pi$ and $\phi_{d2} = -5/8\pi$.	RE, $t \in [1.25, 1.75]$ s $f \in [6.5, 7.5]$ Hz	White	$\mathcal{U}(-7\pi/8, 7\pi/8)$	1
		EEG	$\mathcal{U}(-7\pi/8, 7\pi/8)$	1
Section 4.4.2. Disturbance signal with frequency $f_0 + \Delta f$ but equal time. Phases of disturbance signals are $\phi_{d1} = 5/8\pi$ and $\phi_{d2} = -5/8\pi$.	RE, $t \in [1.25, 1.75]$ s $f \in [6.5, 7.5]$ Hz	White	$\mathcal{U}(-7\pi/8, 7\pi/8)$	1
		EEG	$\mathcal{U}(-7\pi/8, 7\pi/8)$	1

Table 4.1: Overview of simulation parameters.

Two example simulations with different SNR using white Gaussian noise can be seen in Figure 4.1. The two signals have equal amplitude and a relative phase of $\pi/2$.
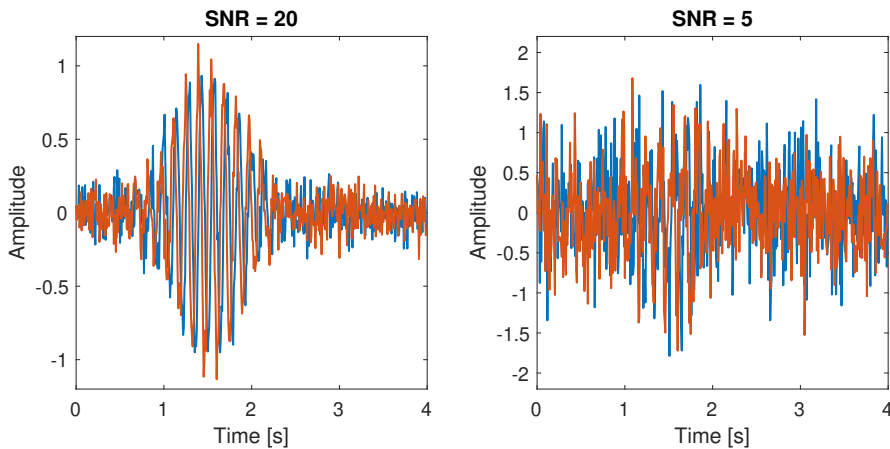
Figure 4.1: Two signals (blue and orange) of equal amplitude with phase-difference $\pi/2$ with added Gaussian white noise.

4.1.2 EEG noise model

EEG noise was simulated in accordance to the procedure described in Barzegaran et al. [15]. The noise was modelled to consist of alpha- $(n_\alpha^{(i)})$, 1/f- $(n_{1/f}^{(i)})$ and white measurement noise $(n_e^{(i)})$, such that the local noise in one channel was given by

$$n_{\text{local}}^{(i)}(t) = n_\alpha^{(i)}(t) + n_{1/f}^{(i)}(t) + n_e^{(i)}(t). \tag{4.4}$$

This noise was used in the SNR definition in Equation 4.3 for the EEG-simulations.

However, the noise that was used in the simulated signals in Equation 4.1 was furthermore mixed across the channels to imitate source leakage. The total noise in channel 1 was then given by

$$n_1(t) = n_\alpha^{(1)}(t) + H_\alpha n_\alpha^{(2)}(t) + n_{1/f}^{(1)}(t) + H_{1/f} n_{1/f}^{(2)}(t) + n_e^{(1)}(t), \tag{4.5}$$

and vice versa in channel 2, where H_α and $H_{1/f}$ are mixing constants. The spectral density of the total noise and the resulting squared coherence between the channels are seen in Figure 4.2. In Figure 4.3 two simulations using EEG noise can be seen for different SNR.
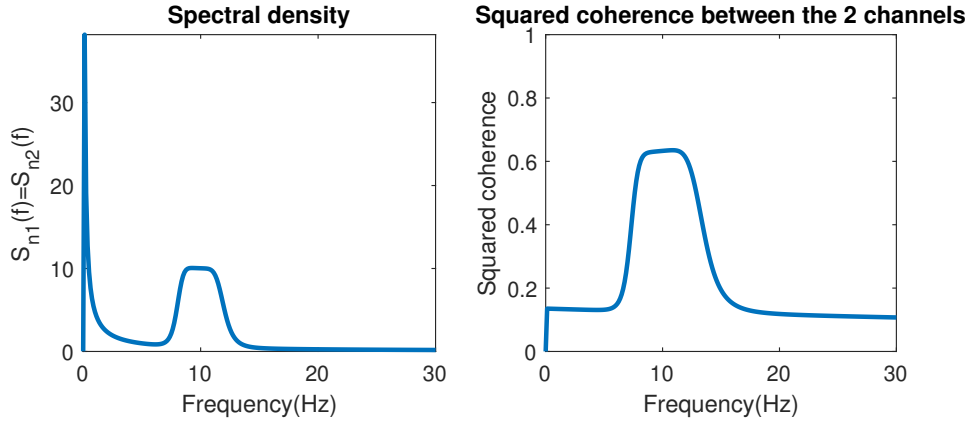
Figure 4.2: To the left: the spectral density of the total EEG noise in Equation 4.5. To the right: the coherence between the total noise in the two channels.

4.2 Estimation of signal scaling parameter σ

In order to investigate the performance of the ScRe-Spec in Algorithm 3 using iterative ($J = 4$) or non-iterative ($J = 1$) estimation and different concentration measurements, simulations using white Gaussian noise and EEG noise were made. In the iterative estimations, the maximum number of iterations in Algorithm 3 was set to $J = 4$, and in the non-iterative estimations it was set to 1. The simulated signal amplitudes were $A_1 = A_2 = 1$, and the relative phase $\Delta\phi$ between the signals was randomly drawn from $\mathcal{U}(-\frac{7\pi}{8}, \frac{7\pi}{8})$ in each trial. The initial window function parameters λ_j were randomly drawn from $\mathcal{U}(30, 70)$ and the candidate signal scaling parameters were $\sigma_i = 30, 31, ...70$. The concentration of the ScRe-Spec was evaluated over the whole spectrogram.
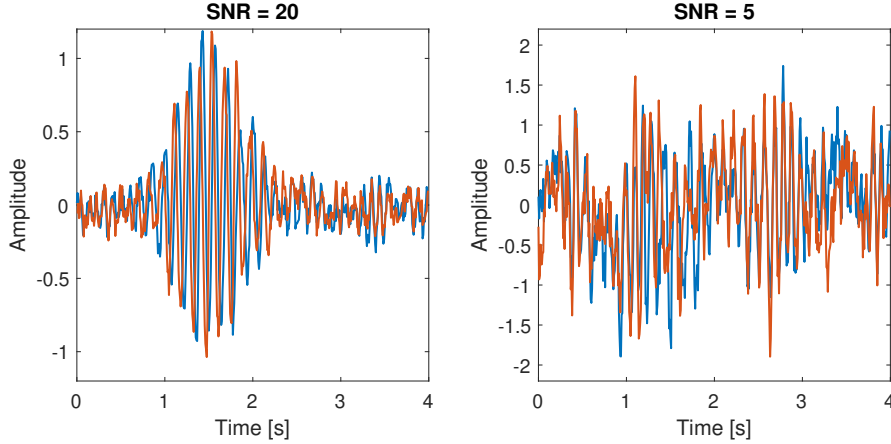
Figure 4.3: Two signals (blue and orange) of equal amplitude with phase-difference $\pi/2$ with added EEG noise according to Equation 4.5.

In Figure 4.4(a) and 4.5(a), the percentage of correctly estimated σ is plotted against SNR for white noise and EEG noise respectively. In (b) the corresponding mean square errors (MSE) are plotted, where the MSE of σ is defined as $MSE = \frac{1}{M} \sum_{m=1}^{M} (\sigma - \hat{\sigma}_m)$, where m denotes the m:th trial for given SNR.

For both white and EEG noise, we see that the estimations using GI perform poorly for low SNR in comparison to RE and TFC. Non-iterative estimation using both RE and TFC seems to be slightly more accurate, or about as accurate as iterative estimation for low SNR. For low SNR, non-iterative estimation also appears to result in smaller MSE. In the white noise simulations in Figure 4.4, the RE and the TFC using non-iterative estimation result in similar amounts of correct estimations and similar MSE. However, when simulations were made using EEG noise in Figure 4.5, the RE appears to yield slightly more correct estimations for SNR larger than 5, whereas the TFC measurement resulted in smaller MSE for low SNR.

The reason for this can be seen in Figure 4.6, where histograms of the estimated signal scaling parameters $\hat{\sigma}$ using non-iterative estimation with different concentration measurements for SNR=-5 using EEG noise are shown. The RE seem to be slightly more biased towards shorter estimations than the TFC, and more often picks the smallest possible candidate σ_i.

From these simulations we draw the conclusion that non-iterative estimation of σ, in addition to being computationally faster, is also generally more robust than iterative estimation. As GI gave inaccurate estimations for low SNR, RE or TFC seem to be the better choices for the σ-estimation part of the algorithm. As only 300 simulations were used for each SNR, it is difficult to know whether one method is significantly better than the other. As the RE is the more conventional choice for evaluating the ScRe-Spec, this is the measurement that was chosen for this step in the algorithm as well.
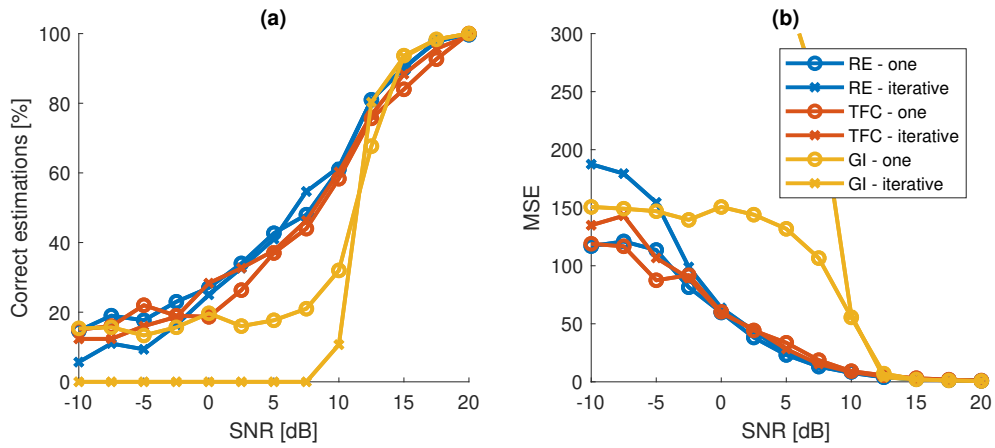
Figure 4.4: The simulations were made using white Gaussian noise. In (a), the percentage of correctly estimated σ is plotted against SNR. The signal scaling parameter is considered to be correctly estimated if $\hat{\sigma} \in [49, 51]$. In (b) the corresponding MSE is show.
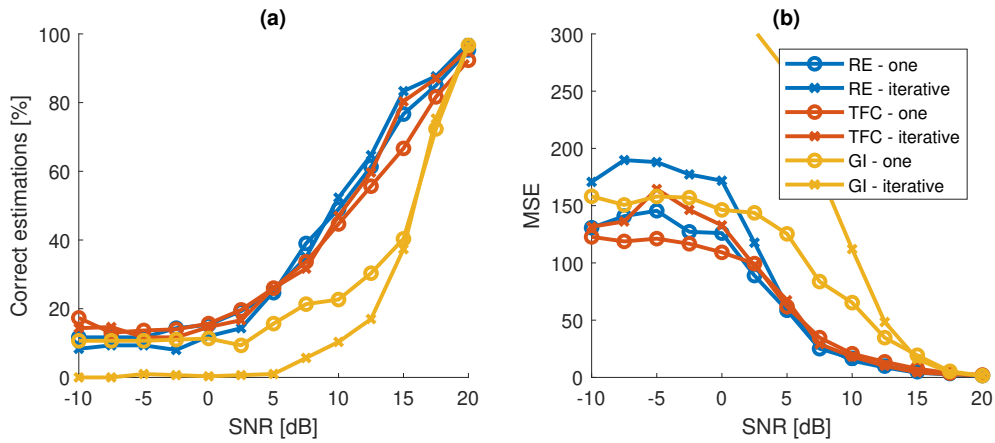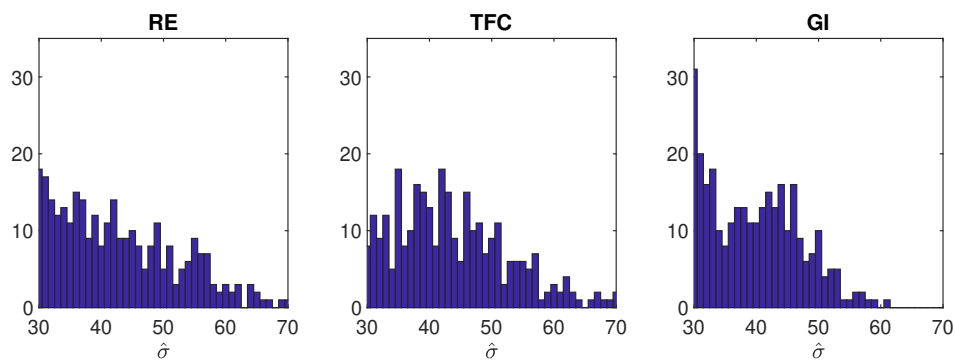

Figure 4.5: The simulations were made using EEG noise. In (a), the percentage of correctly estimated σ is plotted against SNR. The signal scaling parameter is considered to be correctly estimated if $\hat{\sigma} \in [49, 51]$. In (b) the corresponding MSE is shown.

Figure 4.6: Histograms of the estimated signal scaling parameter $\hat{\sigma}$ for SNR = -5.

4.3 Estimation of time-lag k

In order to investigate how the σ-estimation affects the estimation of k, the MPR was evaluated for three different window scaling parameters, $\lambda = \hat{\sigma} = 40, 50, 60$. The aim was moreover to investigate which concentration measurement of RE, TFC and GI result in most robust estimations. The signal amplitudes were as before set to $A_1 = A_2 = 1$ and the candidate time-lags were $k_i = -9, -8, ..., 9$ corresponding to phase-lags between -0.9844π and 0.9844π. The amplitudes were assumed to be correctly estimated, such that A_1 and A_2 in the reassignment vectors in Equation 2.13 were set to 1.

4.3.1 White noise simulations

For the white noise simulations, the phase lags were randomly generated from $\mathcal{U}(-\frac{7\pi}{8}, \frac{7\pi}{8})$. In Figure 4.7a, the percentage correctly estimated time-lags $\hat{k}$ is plotted against SNR for different concentration-measurements, and different window scaling parameters. The estimation is considered to be correct if the error $|k - \hat{k}|$ is less than 1. Three things are especially interesting in these plots.

1. The RE and the TFC perform equally well using a matched window, i.e. $\lambda = \hat{\sigma} = 50$.

2. When σ is under-estimated, the accuracy drops for higher SNR, where the TFC is least affected.

3. When σ is over-estimated, the accuracy drops for higher SNR, where the GI is least affected and RE and TFC perform equally.

The same drop in accuracy occurs under the no noise circumstances as illustrated in Appendix A.2. Although it at first appears strange, it is most likely the product of violating the matched window assumption in the MPR. The different concentration measurements seem to be more or less affected by this violation. Histograms of the estimation errors $(k - \hat{k})$ when $\hat{\sigma} = 40$ and SNR $= 15$ are shown in Figure 4.7c. It can be seen that all concentration measurements (mostly) result in estimation errors between -2 and 2 for this SNR. For the GI, no perfect estimations are made and most estimations are two samples off. For the RE, few perfect estimations are made and most estimations are one or two samples off. For the TFC, most estimations are one sample off. The same behaviour occurs when the window is too long, with the only difference being that GI is somewhat less affected.

This is not a major drawback for any of the concentration measurements as the error is limited to two samples. From the MSE plots in Figure 4.7b, we see that RE and TFC perform approximately equal. When the SNR decreases, as in Figure 4.7d, the problem becomes negligible, and the number of perfect estimations increases for all concentration measurements.
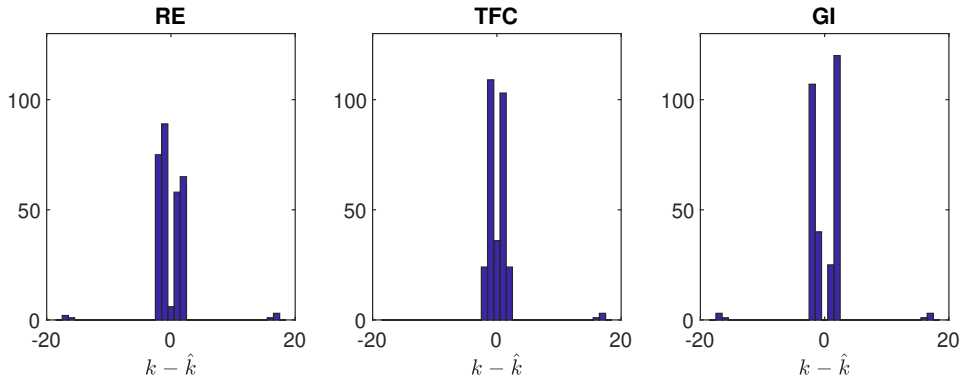
Furthermore, the simulated data was divided into two classes; they could either have negative or positive relative phase. In order to investigate the performance of a binary
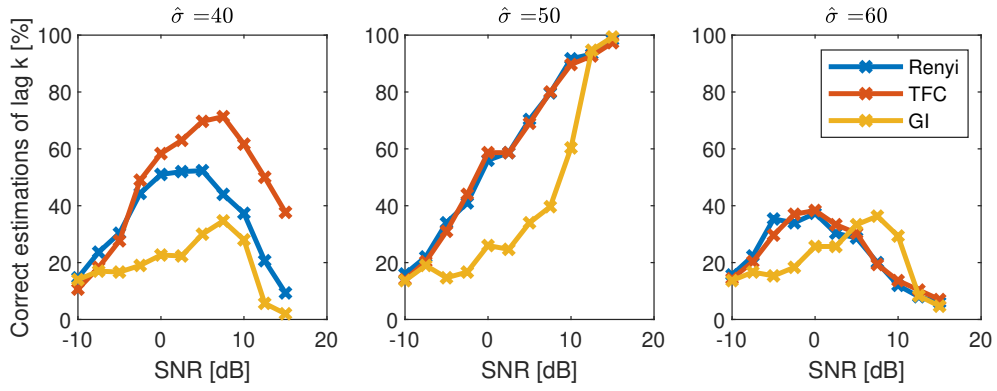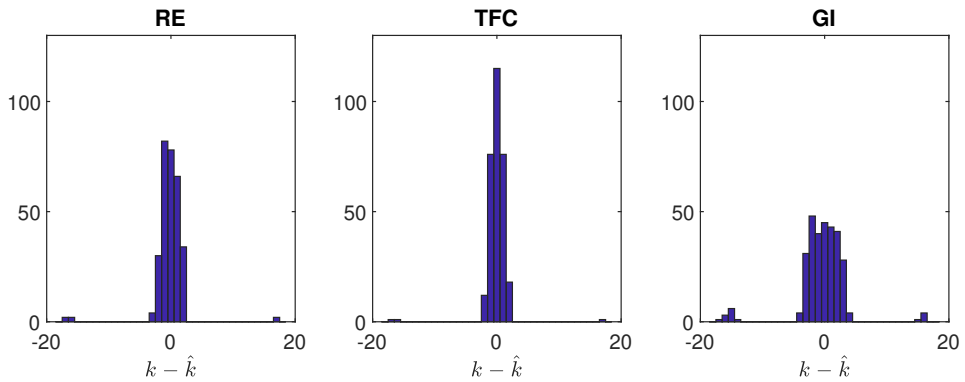
(a) The percentage of correctly estimated time-lags k against SNR.
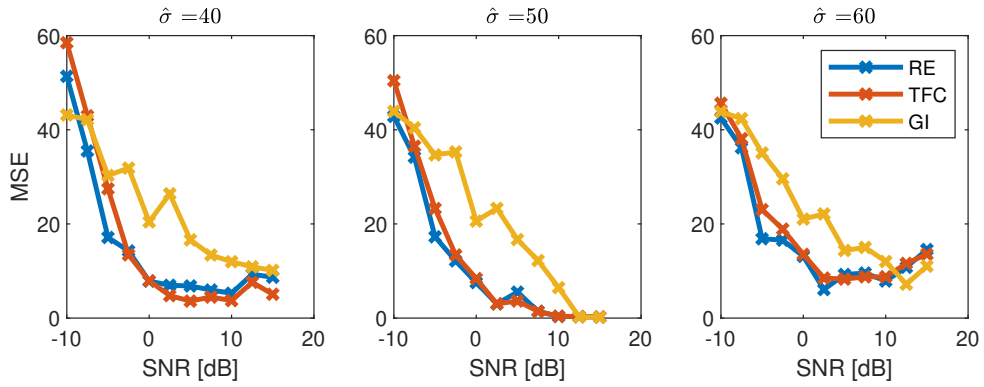
(b) Resulting MSE of the time-lag estimations k against SNR.

(c) Histograms of the time-lag estimation error $k - \hat{k}$ for SNR = 15, and $\hat{\sigma} = 40$.

(d) Histograms of the time-lag estimation error $k - \hat{k}$ for SNR = 5, and $\hat{\sigma} = 40$.

Figure 4.7: White noise simulation results for estimation of k.

classifier, the true positive classification rate (TPR) is plotted against the false positive rate (FPR) for different thresholds in a so called receiver operating characteristic (ROC) curve. In Figure 4.8a and 4.8b, ROC curves are plotted for different estimated σ. In these plots, the MPRs ability to correctly classify the time-lag k as either positive or negative is investigated. For SNR=-5, we see that the RE is preferable. As the SNR increases however, the RE and TFC perform equally well.
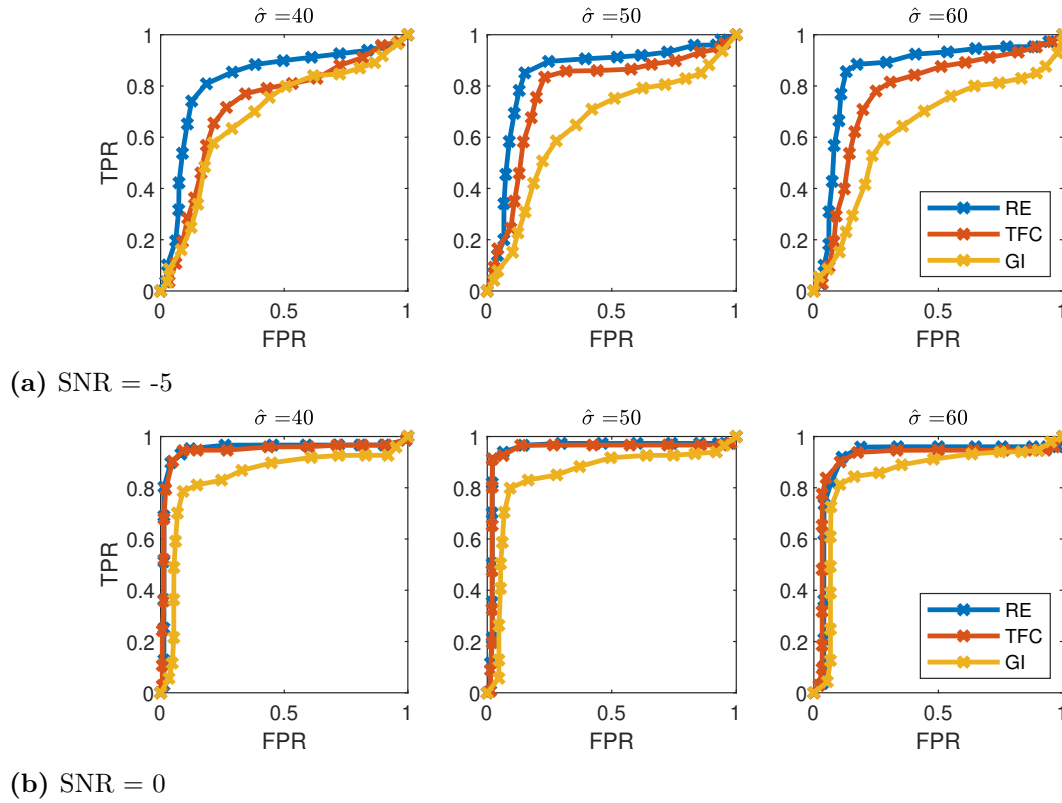

(a) SNR = -5

(b) SNR = 0

Figure 4.8: ROC curves for a binary classifier, where the time-lags are classified as either negative or positive.

4.3.2 EEG noise with signals in phase

Due to source leakage, the noise in two EEG channels will have a phase difference of zero. In order to investigate the different concentration measurements sensitivity to this, the simulations were divided into the following two cases:

1. The signals have a relative phase of zero, $\Delta\phi = 0$, just as the noise.

2. The signals have a relative phase that is non-zero and positive, such that $\Delta\phi \sim \mathcal{U}(\pi/8, 7\pi/8)$.

In Figure 4.9a, the zero-lag simulation results can be seen. The percentage of correct estimations for all concentration measurements are high even for low SNR. This can be explained by the additional zero-lag synchronization in the noise. For higher SNR when $\hat{\sigma} = 40$ and $\hat{\sigma} = 60$, the proportion decreases due to violating the matched window assumption discussed previously. In these cases the TFC seem to perform better than

the other measurements. However, for low SNR the TFC performs poorly, and gets relatively large MSE as seen in Figure 4.9b. The cause of this is seen in Figure 4.9c, where the errors are more smeared out compared to the other measurements. Most likely, the TFC is less sensitive to the zero-phase lag caused by the spectral leakage, but instead makes more random estimations.

As before, the GI perform poorly for high SNR. As its MSE is relatively low, this indicates that it consistently estimates lags close to zero.

The RE is somewhere in between the TFC and GI, as it perform similarly to GI for low SNR and similarly to TFC for high SNR, when $\hat{\sigma} = 50, 60$.
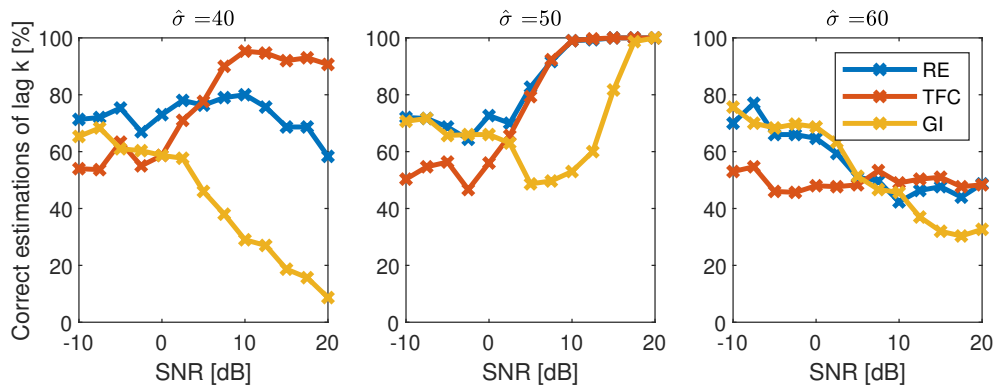
(a) The percentage of correctly estimated time-lags k against SNR.
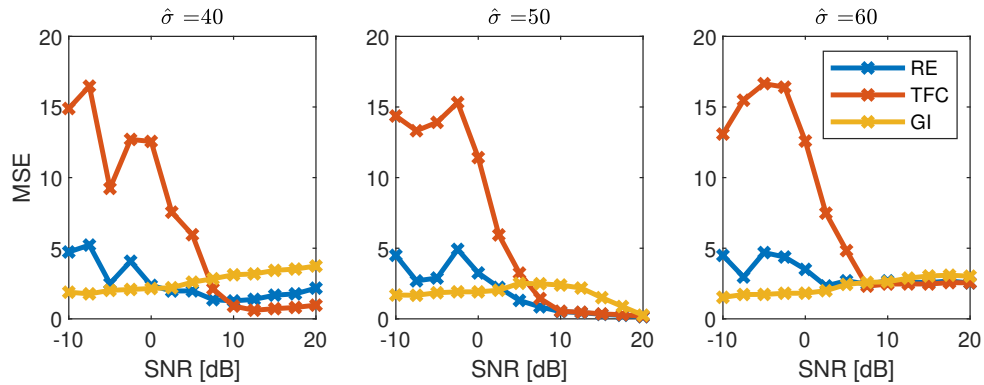
(b) Resulting MSE of the time-lag estimations k against SNR.
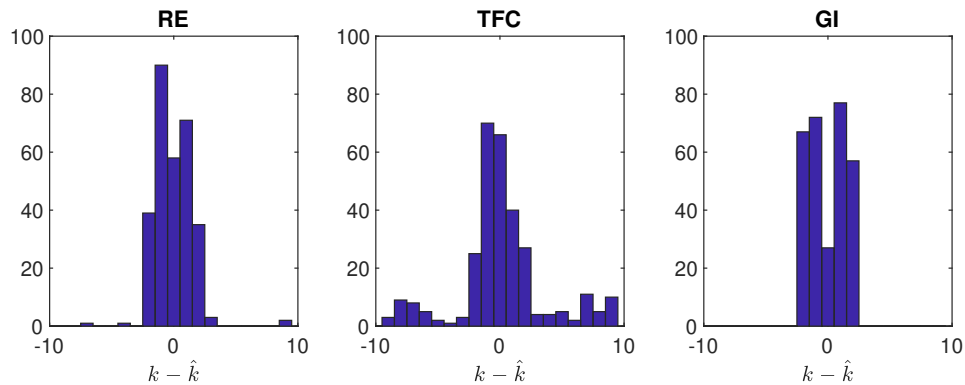
(c) Histograms of the time-lag estimation error $k - \hat{k}$ for SNR = 0, and $\hat{\sigma} = 40$.

Figure 4.9: EEG noise simulation results for estimation of k. The relative phase was zero.

4.3.3   EEG noise with signals out of phase

In these simulations the relative phase was generated as $\Delta\phi \sim \mathcal{U}(\pi/8, 7\pi/8)$. From the percentage correct estimations in Figure 4.10a, we see similar results to the white noise simulations. The MSE plots in 4.10b seem to differ however. In comparison to the white noise simulations, the GI result in overall lower MSE relative to the other measurements. The TFC result in somewhat higher MSE for low SNR.

From the histograms in Figure 4.10c and 4.10d, we see that most time-lags are under-estimated for SNR=-5. This is explained by the zero-phase lag in the EEG noise. Once again we see that the TFC is least affected by this. When the SNR=7.5, we see that the GI still is under-estimating the time-lag, whereas the RE and the TFC make fairly accurate estimations.

4.3.4   Negative or positive phase classification with EEG noise

In order to construct ROC curves for the binary classifier previously presented, EEG simulations were made with relative phases generated from $\mathcal{U}(-\frac{7\pi}{8}, \frac{7\pi}{8})$. The resulting ROC curves for different SNR and different estimated signal scaling parameters $\hat{\sigma}$ can be seen Figure 4.11. For really low SNR, when SNR = -5, the GI seems to make slightly more correct classifications. When SNR increases to SNR=0, the TFC gets slightly more accurate than both the RE and the GI for $\hat{\sigma} = 50$ and $\hat{\sigma} = 60$. As the SNR increases even more, to SNR=5 and above, the RE and the TFC becomes equally accurate.

4.3.5   Time-lag estimation conclusions

From the simulations we draw the following conclusions. In both the white noise and EEG noise simulations, the GI displayed poor performance in comparison to the other measurements.

Under the white noise circumstances, the RE and TFC displayed similar performance. When the matched window assumption was violated and the window was smaller, the TFC resulted in a higher number of correct estimations estimations than the RE for large SNR, but the RE did not make errors larger than 2 samples. From the ROC curves, the RE displayed slightly better performance than the TFC for low SNR.

Under the EEG noise circumstances, the RE seemed to be slightly more sensitive than the TFC to zero-phase source leakage. However, maybe because of this, the TFC resulted in a wider variety of estimations and displayed larger MSE for low SNR. In the ROC curves their performance was approximately equal.

In conclusion the TFC was on par with the RE in terms of estimating time lag in the MPR. It is therefore difficult to say which measurement is more suitable for this use. As the RE is the more conventional choice for evaluating reassigned spectrograms, it was used in the two-step algorithm in the following simulations.
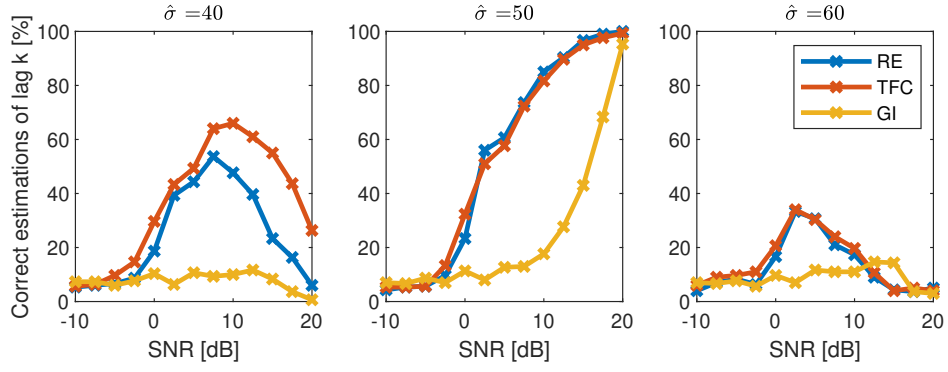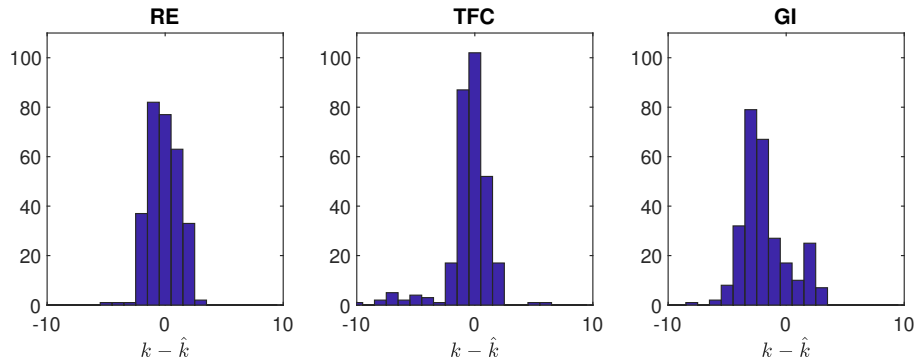
(a) The percentage of correctly estimated time-lags k against SNR.
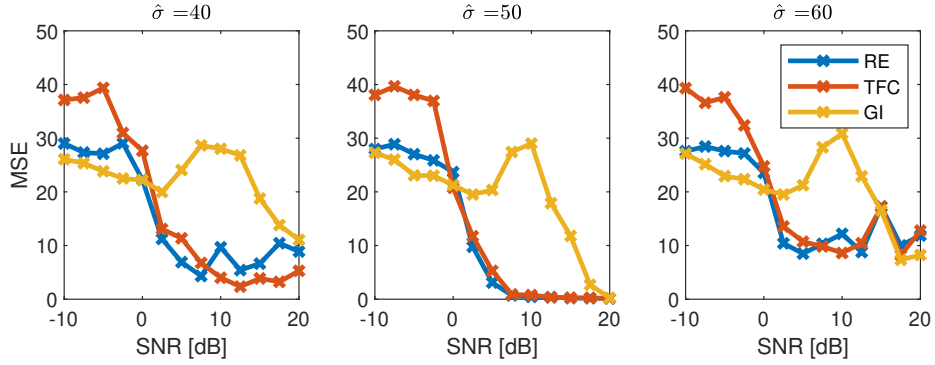
(b) Resulting MSE of the time-lag estimations k against SNR.
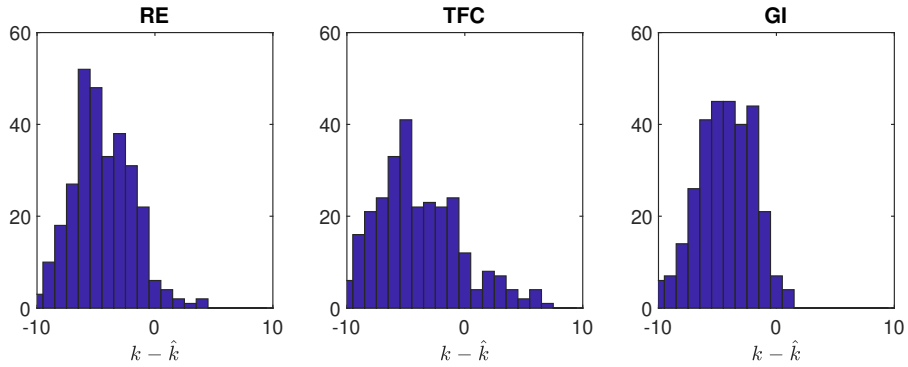
(c) Histograms of the time-lag estimation error $k - \hat{k}$ for SNR = -5, and $\hat{\sigma} = 40$.

(d) Histograms of the time-lag estimation error $k - \hat{k}$ for SNR = 7.5, and $\hat{\sigma} = 40$.

Figure 4.10: EEG noise simulation results for estimation of k. The relative phase was randomly generated from $\mathcal{U}(\pi/8, 7\pi/8)$.

(a) SNR = -5

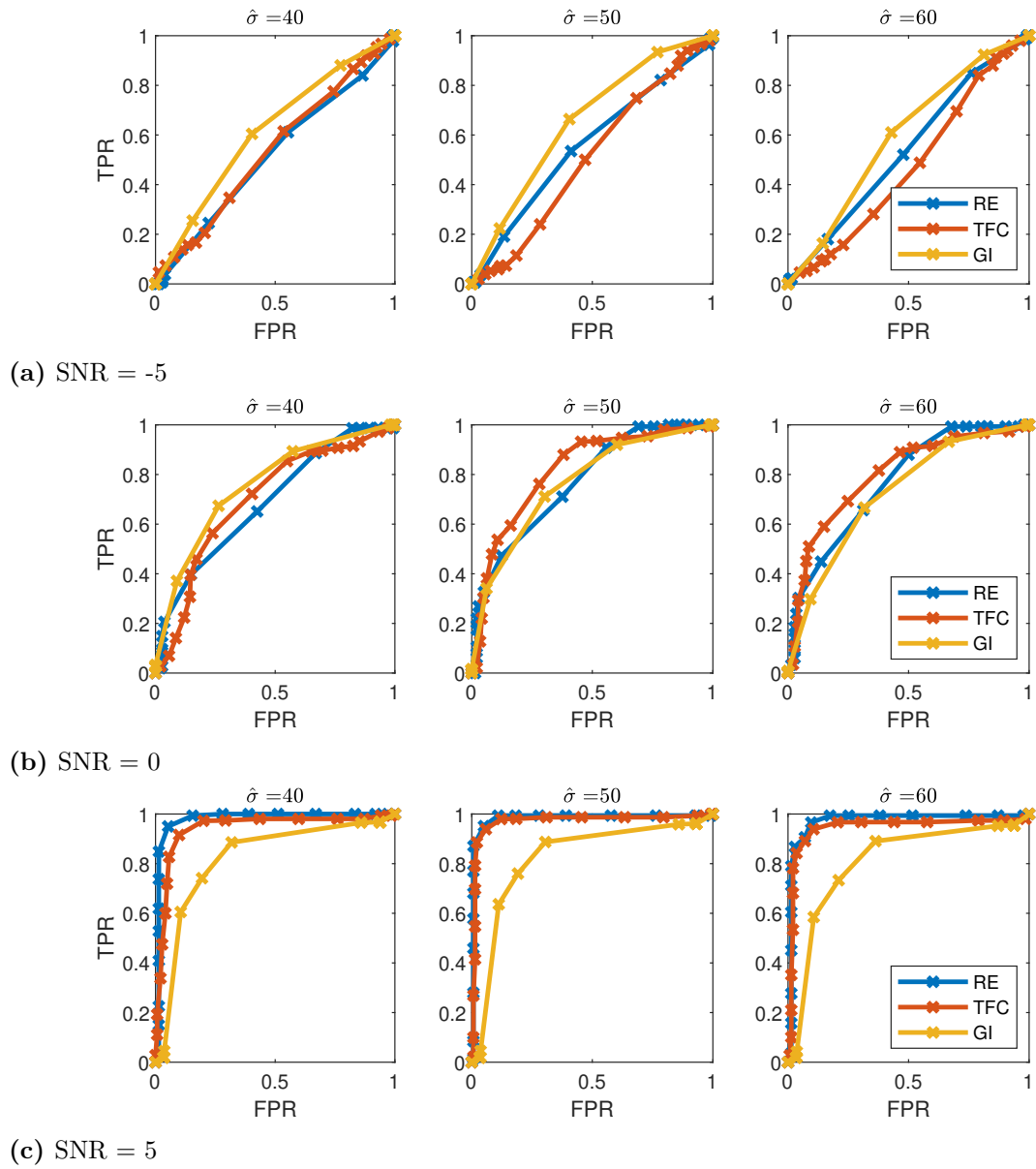**(b)** SNR = 0

(c) SNR = 5

Figure 4.11: ROC curves for a binary classifier, where the time-lags are classified as either negative or positive.

4.4 Disturbance simulations - comparison with other methods

Next, the two-step algorithm was compared to two other relative phase-estimation methods presented in Section 2.3.2, the Hilbert transform and Pearson's linear correlation coefficient (CORR). These were evaluated in the same manner as the MPR, i.e. different time-shifts k_i were applied to the second signal and then the optimal time-shift was chosen as the estimation. For the Hilbert transform, the mean value of the instantaneous relative phases in Equation 2.29 was calculated for each time-shift k_i. The lag which gave minimum value was chosen as the estimation. The algorithm was furthermore compared to Pearson's linear correlation coefficient given in Equation 2.32. The time-lag which gave maximum correlation was used as the estimation.

In Figure 4.12, the correlation and Hilbert transform based measurements are plotted when evaluated for a simulated signal without noise. We see that the measurements either have a peak or a valley at the lag corresponding to the true relative phase. In the Figure, the true phase was $\Delta\phi = -0.1\pi$.
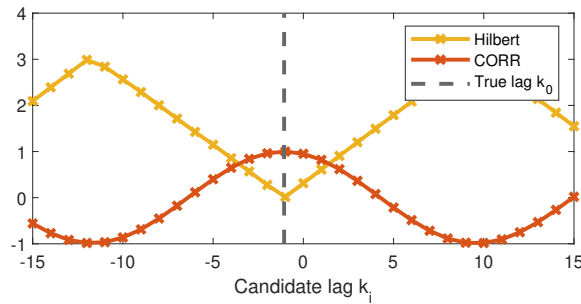

Figure 4.12: Illustration of how the time-lag, corresponding to the relative phase $\Delta\phi$, was estimated.

The RE in the two-step algorithm was evaluated over $t \in [1.25, 1.75]$ s and $f \in [6.5, 7.5]$ Hz, whereas the other measurements were evaluated over $t \in [1.25, 1.75]$ s. In the two-step algorithm the candidate scaling parameters were $\sigma_i = 30, 31, ..., 70$, and the amplitudes were estimated from the spectrogram. For all methods the candidate time lags were $k_i = -9, -8, ..., 9$. The signal of interest was simulated as before, with $A_1 = A_2 = 1$, $\Delta\phi \sim \mathcal{U}(-7\pi/8, 7\pi/8)$.

4.4.1 Disturbance in time

In addition to the simulated signal of interest with centre time $t_0 = 1.51$ s, identical disturbance signals with centre times $t_{d0} \in [1.51, 3.0]$ s were included. In channel 1, the phase of the disturbance was $\phi_{d1} = 5\pi/8$ and in channel 2 it was $\phi_{d1} = -5\pi/8$. An example is shown in Figure 4.13. White Gaussian noise, as well as EEG noise, was added to evaluate the different relative phase estimation methods.

The white noise simulation results are seen in Figure 4.14. In (a), the percentage correct estimations are plotted against SNR when the disturbance signal was close to
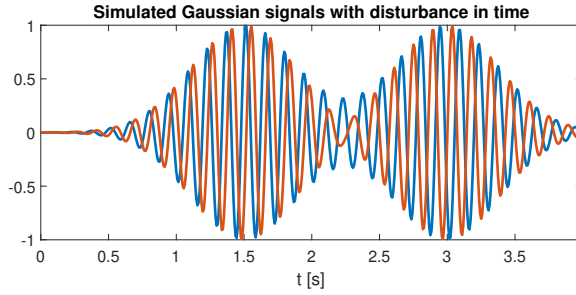
Figure 4.13: Example of simulated signals with disturbance signals at $t_{d0} = 3.0$ s.

the signal of interest. In (b) the disturbance signal was further away from the original signal, making it easier for the methods to differentiate between the two. In (c), the percentage correct estimations are plotted against a range of disturbance centre times t_{d0} when the SNR is kept constant at $SNR = 5$. The corresponding MSE of all these plots are seen in Figure 4.15.

The same kind of plots but with EEG noise can be seen in Figure 4.16 and Figure 4.17.
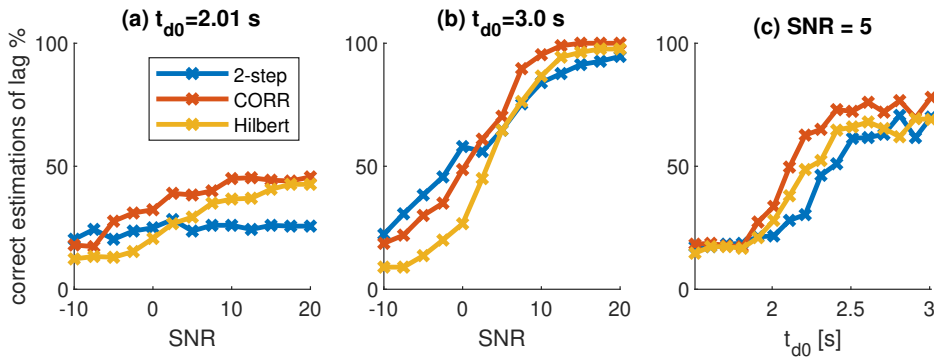

Figure 4.14: Results from white noise simulations. In (a) and (b), the percentage correct estimations against SNR is shown. In (a), the disturbance signal is close in time to the signal of interest, and in (b) it is far away. In (c), the SNR is kept constant, and the percentage correct estimations are plotted against the centre time of the disturbance signal. The centre time of the signal of interest is $t_0 = 1.51$ s.
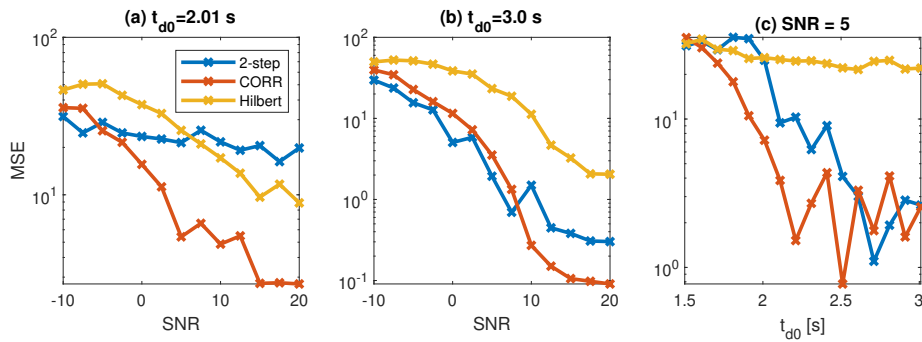

Figure 4.15: Corresponding MSE of the results in Figure 4.14.

From the white noise simulations in Figure 4.14, we see that all measurements, but especially the 2-step algorithm, perform poorly when the disturbance signal is close

in time. When the disturbance is far away, the two-step algorithm perform slightly better for low SNR. The corresponding MSE in 4.15 reveal that although the Hilbert transform gave more correct estimations than the two-step algorithm for high SNR, the estimations from the two-step algorithm resulted in smaller MSE for the simulations in (b) and (c).

In Figure 4.14(c), we see that the two-step algorithm is about equally bad for all $t_{d0} < 2.0$ s when SNR $= 5$. Even though the RE measurement window was set to $t \in [1.25, 1.75]$ s, the algorithm wasn't able to perform any better for disturbance signals outside the window at $t_{d0} = 2.0$ s, than for signals inside the window. Furthermore, the performance of the two-step algorithm plateaus for $t_{d0} > 2.5$ s, which is around 1 s after $t_0 = 1.51$ s. The other methods seems to plateau slightly before this. Similar results are seen in the EEG simulations Figure 4.16 and 4.17.
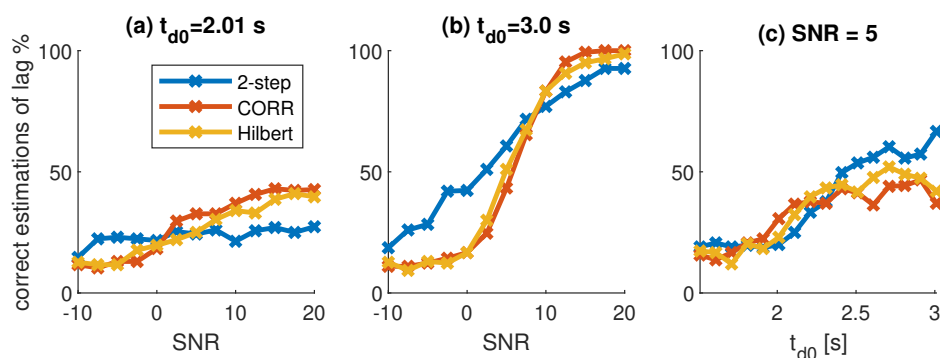

Figure 4.16: Results from EEG noise simulations. In (a) and (b), the percentage correct estimations against SNR is shown. In (a), the disturbance signal is close in time to the signal of interest, and in (b) it is far away. In (c), the SNR is kept constant, and the percentage correct estimations are plotted against the centre time of the disturbance signal. The centre time of the signal of interest is $t_0 = 1.51$ s.
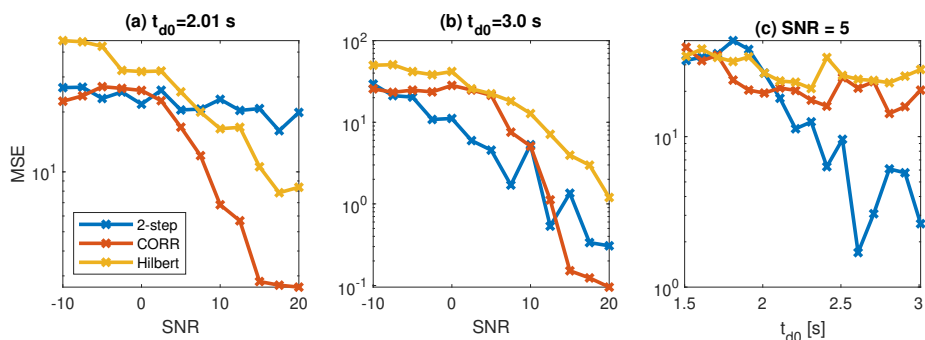

Figure 4.17: Corresponding MSE of the results in Figure 4.16.

We try to gain additional insight about the two-step algorithm by looking at at Figure 4.18, where the cross-spectrograms and the optimal MPR of the same kind signals are shown. The true time-lag was $k_0 = 0$, which corresponds to $\Delta\phi = 0$, and no noise was added. Although the signals are noise free and the matched window assumption is fulfilled, the MPR have issues estimating the correct time-lag due to the disturbance signal. The estimation errors in the figure is no more than 2 samples. The exact same estimations were made using the TFC instead of the RE.
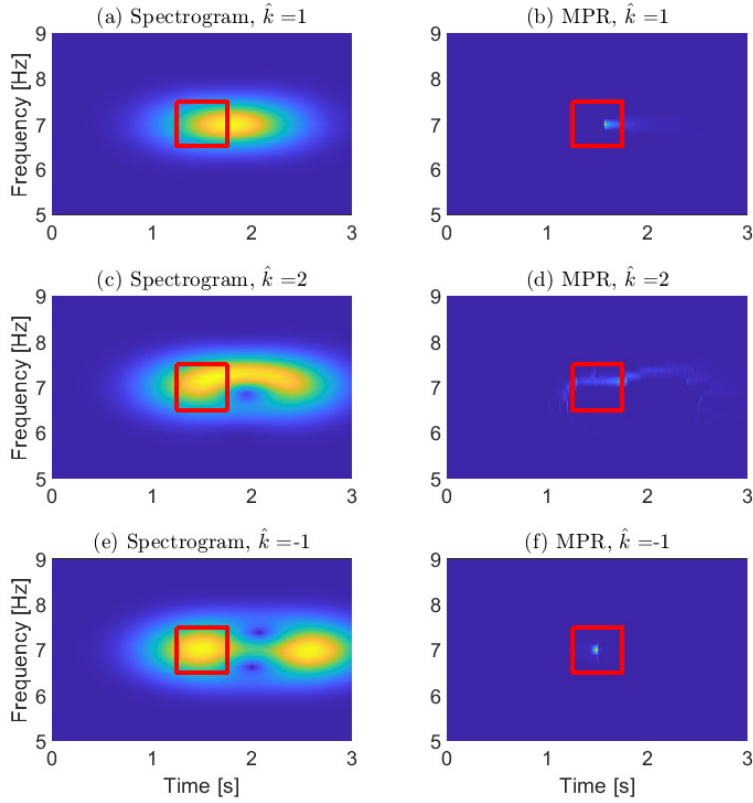
Figure 4.18: The cross-spectrogram and corresponding MPR for a estimated time-lag $\hat{k}$ for different disturbance times t_{d0}. The signals were simulated without noise, and $k_0 = 0$. In all plots $\lambda = \hat{\sigma} = 50$. In (a)-(b): $t_{d0} = 2.01$ s. In (c)-(d): $t_{d0} = 2.26$ s. In (e)-(f): $t_{d0} = 2.51$ s. The red squares illustrate the window over which the RE was evaluated.

4.4.2 Disturbance in frequency

Similarly to the simulations in Sandsten et al. [5], disturbance signals with centre frequency $f_{d0} \in [4, 10]$ Hz, but centre time $t_{d0} = t_0 = 1.51$ s were included in these simulations. As in the previous simulations, the phases were $\phi_{d1} = 5\pi/8$ and $\phi_{d1} = -5\pi/8$. An example of the resulting signals are shown in Figure 4.19, where no noise was added. In Figure 4.20 and 4.21, the results from the white noise and EEG noise simulations are shown.
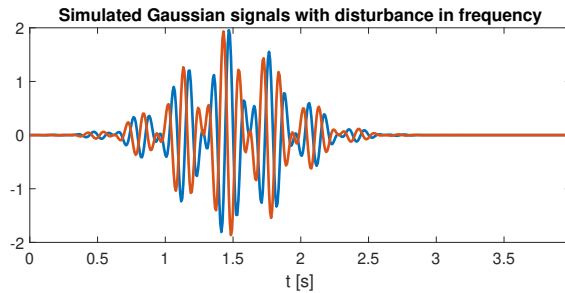

Figure 4.19: Example of simulated signals with disturbance signals at $t_{d0} = 1.51$ s with centre frequency $f_{d0} = 10$ Hz.

From both the white and EEG noise simulations, we see that the two-step algorithm is superior to the other methods. This is unsurprising as the other methods are unable to separate between signals in frequency domain, which was also noted in Sandsten et al. [5]. Although the measurement window was set to $f \in [6.5, 7.5]$ Hz, we see from 4.20(a) and 4.21(a) that the two-step method was unable to make correct estimations when the disturbance was just outside the window, when $f_{d0} = 7.75$ Hz. When SNR $= 10$ in Figures 4.20(c) and 4.21(c), we see that the two-step method is able to make correct estimations for $f_{d0}8$ Hz and $f_{d0}6$ Hz, a bit outside the measurement window. The number correct estimations plateau about $f_{d0} > 8.5$ Hz and $f_{d0} < 5$ Hz.
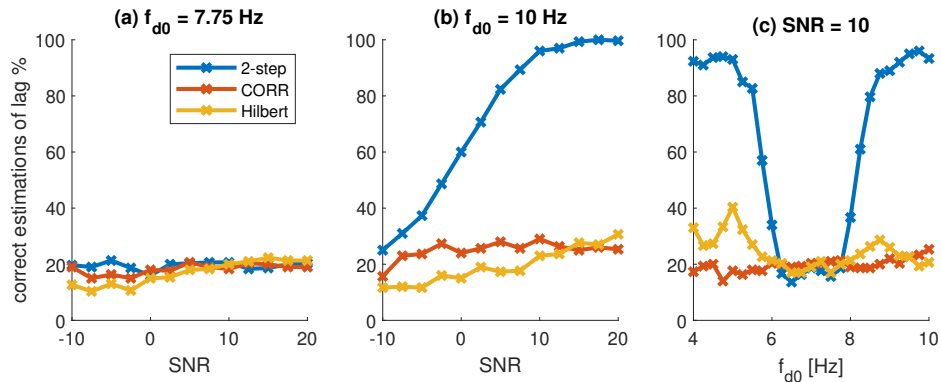

Figure 4.20: Results from white noise simulations. In (a) and (b), the percentage correct estimations against SNR is shown. In (a), the disturbance signal is close in frequency to the signal of interest, and in (b) it is far away. In (c), the SNR is kept constant, and the percentage correct estimations are plotted against the centre frequency of the disturbance signal. The centre frequency of the signal of interest is $f_0 = 7.0$ Hz.

Figure 4.21: Results from EEG noise simulations. In (a) and (b), the percentage correct estimations against SNR is shown. In (a), the disturbance signal is close in frequency to the signal of interest, and in (b) it is far away. In (c), the SNR is kept constant, and the percentage correct estimations are plotted against the centre frequency of the disturbance signal. The centre frequency of the signal of interest is $f_0 = 7.0$ Hz.
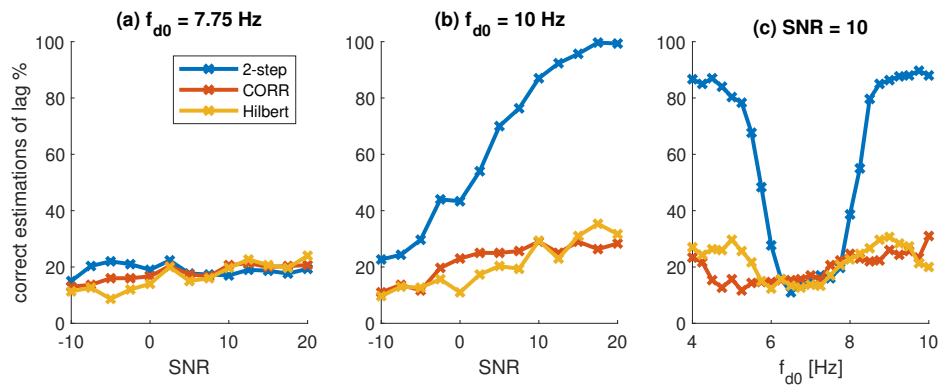
4.4.3 Discussion & conclusions

From the simulations we draw the conclusion that the two-step algorithm make superior estimations compared to the other measurements when a disturbance signal in

frequency is present. When a disturbance signal close in time is present, the two-step algorithm only outperforms CORR and the Hilbert transform when the SNR is low. When SNR is high, and the disturbance signal is adequately far away from the signal of interest, the two-step algorithm make fewer correct estimations than the other methods. However, it still results in smaller MSE than the Hilbert transform. This indicates that the estimations from the two-step algorithm are more concentrated around the true lag than the estimations using the Hilbert transform.

From these and previous simulations, two potential causes for the algorithm's low performance in high SNR have been observed:

1. Slight deviations to the lag-estimations due to incorrect estimations of the signal scaling parameter σ by the ScRe-Spec, which leads to a violation of the matched window assumption in the MPR.

2. The disturbance signal being too close to the signal of interest, violating the assumed signal model in the MPR in Equation 2.20.

Although the algorithm doesn't appear to be very robust against violating these assumptions in high SNR, the errors are small, and the algorithm outperforms other methods when SNR is low. The two-step method therefore seems to be a suitable alternative to the other relative phase estimation methods when the signals can be assumed to be oscillating Gaussian transients.

From the simulations we also observed that the algorithm was unable to make correct estimations when the disturbance signal was too close to the signal of interest, even though the disturbance centre time and frequency was outside the measurement window. As only one window size and one signal scaling parameter were used in these simulations, it remains unclear how the evaluation window affects the estimations, and if a better window could be chosen.

Some other differences between the two-step algorithm and the other methods are also worth noting. As the two-step algorithm involves several FFT-computations and the reassignment involves computations of rather large matrices, the two-step method is significantly slower than the other methods. This is of course a huge drawback in certain settings. To use this method, some prior information about the signal is needed, such as time and frequency to determine a suitable window, frequency to determine suitable candidate time-lags and signal scaling parameter to determine suitable candidate sigmas.

However, with the increased computation time also comes more information. The two-step algorithm is able to provide additional information, such as the signal scaling parameter and the time and frequency of the maximum peak in the cross-spectrogram.

In future investigations the algorithm could also be compared to the coherence, which similarly to correlation is used as a measurement of functional connectivity. As the coherence measurement assumes stationary signals, which the studied transients definitely isn't, this measurement was excluded from the simulations.

5 Real data examples

After a final two-step algorithm had been constructed, it was tested on two types of real EEG data.

5.1 Phase-estimation in multi-channel EEG with flickering light

Three EEG data sets called bl1, bl2 and bl3 were investigated. The measurements were recorded from 12 channels: F3, Fz, F4, C3, Cz, C4, P3, Pz, P4, O1, Oz and O2. During the recordings, flickering light of 9 Hz was presented in front of a person with closed eyes. The light was present for 1.4 s in bl1, 1.8 s in bl2 and 1.0 s in bl3. The data was recorded with a sampling frequency of 256 Hz.

This kind of flickering light give rise to detectable event related oscillations (ERO) in the brain, containing the same frequency as the presented light. One would expect the ERO to first arise at the back of the head, as the primary visual cortex is located there. Then the signal would spread and appear in other parts of the brain.

Time-frequency representations of the O2-channels are seen in Figure 5.1. For bl1 and bl2, the flickering light signal is strong and visible in the plot. In bl3 it is not.
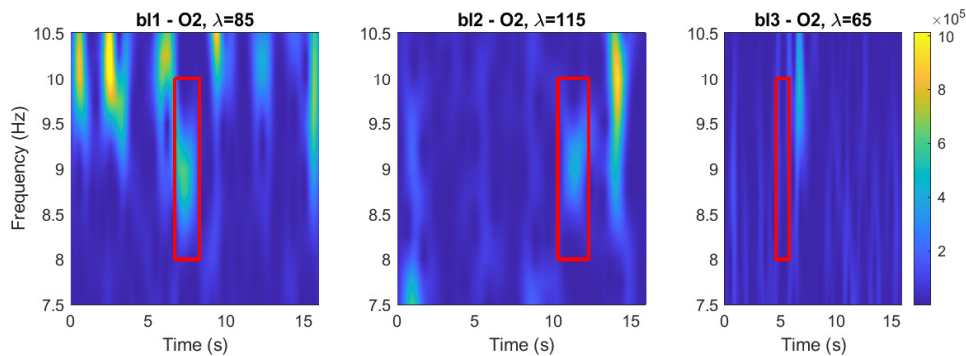

Figure 5.1: Spectrogram of the O2-channel of the different data sets bl1 bl2 and bl3, using different window scaling parameters.

The two-step algorithm was used to estimate the signal lengths and time-lag. The Fourier transform was evaluated in 1024 points and the RE was calculated over a limited area $f \in [f_1, f_2] = [8, 10]$ Hz. As the duration of the flickering lights were known, the RE was calculated over those times and only a small set of candidates were investigated. The data-set specific parameter choices are listed in Table 5.1. The following candidate time-lags were investigated $k_i = -8, -7, ..., 8$, which corresponds to phase-differences between -0.5625π and 0.5625π if the frequency is assumed to be 9 Hz.

Table 5.1: Parameters used for each data set. The corresponding signal scaling parameters in Equation 2.4 as well as the flickering light durations are also listed.

Set	Initial λ	$[t_1, t_2]$	Candidate σ	Corr. lengths	Ref.
bl1	85	$[6.7,\ 8.3]s$	$\{85, 86, ..., 105\}$	$\{1.2095,..., 1.4941\}$ s	1.4 s
bl2	115	$[10.3,\ 12.3]s$	$\{115, 116, ..., 135\}$	$\{1.6364,..., 1.9210\}$ s	1.8 s
bl3	65	$[4.6,\ 5.8]s$	$\{65, 66, ..., 85\}$	$\{0.9249,..., 1.2095\}$ s	1.0 s

All channels were compared to the O2-channel, placed at the back right of the head. Note that, as the algorithm calculates the mean value of two estimated signal scaling parameters, and one channels always was O2, this estimation will have an (unfairly) large influence on these estimations. In order to get a more fair representation of the estimated signals lengths, one should instead use the ScRe-Spec on each individual channel.

The estimated signal lengths are presented in Table 5.2, and the estimated time-lags in Figure 5.2 to 5.4. The signal lengths are slightly longer than the reference flickering light durations for bl1 and bl2. This could be caused by many things. The estimations of the signal-length in O2 could be too long, the signal length definition in Equation 2.4 could be an ill-suited conversion, or the electrical responses could simply be longer. The signal lengths were under-estimated in bl3. This was expected as the signal was difficult to see in Figure 5.1, and the ScRe-Spec is slightly biased towards shorter window lengths in settings with low SNR.

Table 5.2: Estimated signal lengths using the two-step algorithm, where each channel was compared to O2.

Channel pair	bl1	bl2	bl3
F3-O2	1.4799 s	1.9068 s	1.0316 s
Fz-O2	1.4870 s	1.7787 s	0.9676 s
F4-O2	1.3518 s	1.9139 s	0.9534 s
C3-O2	1.4585 s	1.8641 s	0.9320 s
Cz-O2	1.4728 s	1.8641 s	0.9534 s
C4-O2	1.3874 s	1.8925 s	0.9320 s
P3-O2	1.4799 s	1.8427 s	0.9320 s
Pz-O2	1.4728 s	1.8783 s	0.9320 s
P4-O2	1.4372 s	1.8498 s	0.9320 s
O1-O2	1.4656 s	1.8143 s	0.9320 s
Oz-O2	1.4870 s	1.8925 s	0.9392 s
Mean	1.4528 s	1.8634 s	0.9489 s

From the resulting Figures, the patterns in bl1 and bl2 were expected. In both cases the time-lag between F4 and O2 is 4, which corresponds to 15.6 ms or a relative phase of 0.2813π. As the O2 signal wasn't visible in the spectrogram in Figure 5.1, the difficulty of estimating the time-lag increases, and it is expected for the estimations to differ.
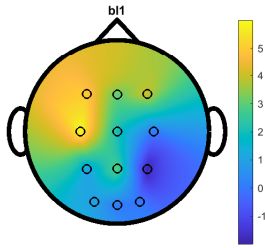
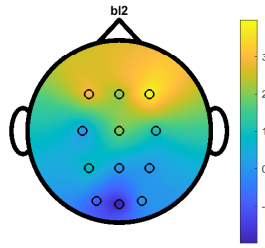**Figure 5.2:** Estimated time-lags compared to O2 in bl1.

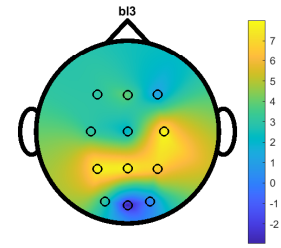**Figure 5.3:** Estimated time-lags compared to O2 in bl2.

Figure 5.4: Estimated time-lags compared to O2 in bl3.

5.2 Classification of two-channel auditory ERO

Next, the algorithm was used on the data set described in Persson [26]. In this data, the subjects were first presented with visual stimulation. After 0.6 seconds, auditory stimulation was presented in either left or right ear. Comparing two EEG oscillations, one on each side of the head, it is possible that the presentation side may affect the relative phase between them. This example aims to explore the possibilities of determining the auditory presentation side from EEG recordings alone, recorded on opposite sides of the head.

5.2.1 Description of data

Data from subject 10 was used, containing recordings from 352 trials and 60 channels. The sampling rate was 1000 Hz during recording, but was later downsampled to 500 Hz. A high-pass filter at 0.1 Hz was applied and the data was baseline corrected using the average. Line-noise at 50 Hz was reduced and artefacts were manually removed. Independent component analysis (ICA) was used to remove other artefacts. A more detailed description of the data acquisition and pre-processing can be found in Persson [26].

5.2.2 Procedure

In contrast to the previous example, the time and frequencies of the EROs were unknown. The first step was therefore to find relevant signals which were induced by the auditory stimulation. In order to estimate relative phase, the signals should be of the same frequency and be phase-synchronized. Although it is uncertain whether the ERO would be of the same frequency in each trial, this was assumed in order to limit the number of possible signal locations.

A relevant frequency interval as well as relevant channels were found through the following procedure:

1. In order to separate between visual and auditory ERO, the data was divided into 'time after visual onset', between 0 and 0.6 s, and 'time after auditory onset' between 0.6 and 2 s. The data-sets were down-sampled to 250 Hz.

2. The data sets were then band-pass filtered. Forward-backward filtering was applied using `filtfilt` in MATLAB, with a 2:nd order Butterworth bandpass filter (that is, a 4:th order IIR filter) using `butter`. Filtering was applied for several 3 Hz frequency intervals, ranging from 2 Hz to 15.5 Hz.

3. The PLI was then calculated between opposite EEG-channels for each frequency band, and was averaged over all trials.

In Figure 5.5, some plots of the PLI for a specific frequency band can be seen. To the left is the PLI during times with visual stimulation and to the right during auditory. As described previously, the PLI was calculated between opposite EEG-channels which explains the symmetry. When the frequency band is $f \in [8, 11]$ Hz in (a), no strong synchronization is present except during visual stimulation.

In (b), when $f \in [9.5, 12.5]$ Hz, there are synchronized oscillations during auditory stimulation exclusively. Some of these are also present in (c), when $f \in [11, 14]$ Hz. therefore FT7-FT8, C3-C4 and AF3-AF4 were chosen as suitable channel-pairs for frequencies between 9 and 14 Hz.

The two-step algorithm parameters were first "calibrated" on the AF7-AF8 trials. A few different λ, evaluation window sizes, candidate signal scaling parameters and candidate time-lags were investigated during this step. Some suitable parameters were then chosen and used on all trials for all three channel-pairs. The RE evaluation window was set to $t \in [0.6, 1.5]$ s and $f \in [9, 14]$ Hz. The data was once again downsampled to $f_s = 250$ Hz. The STFT were evaluated in 1024 points and the initial window scaling parameter was set to $\lambda = 35$. The following candidate scaling parameters were investigated, $\sigma_i = \{25, 26, ..., 40\}$, corresponding to signal lengths between 0.3643 and 0.5828 s.

The aim was classify whether sound was presented in the left or the right ear by estimating the relative phase between corresponding ERO. Keeping the left channel EEG oscillation fix, the right channel was shifted in time in the algorithm. An illustration of this can be seen in Figure 5.6 where the blue signal, called signal 1, is fix. The orange signal called signal 2 has a phase that is $\phi_2 = \phi_1 + \Delta\phi$, where $\Delta\phi > 0$ in the left plot and $\Delta\phi < 0$ in the right. The sound was thus considered to come from the right ear (orange signal) if the estimated time-lag was positive, and from the left ear if the time-lag was negative.

The candidate time-lags investigated were $k_i = \{-9, 8, ..., -1, 1, 2, ..., 9\}$, where the zero-lag was excluded in order to always be able to make a classification. For 9 Hz signals, a time-lag of 9 corresponds to a relative phase of 0.648π, and for 14 Hz signals it corresponds to a relative phase of 1.0008π.
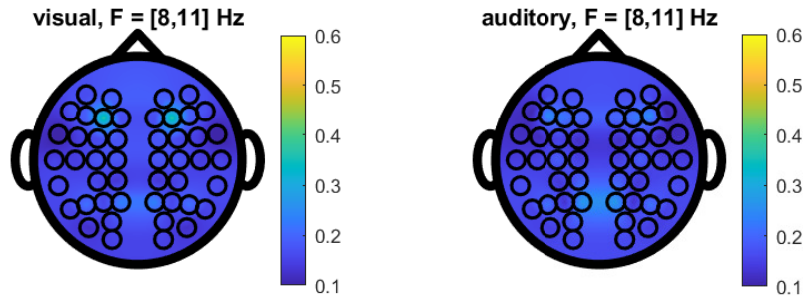
(a) PLI was calculated for filtered signals with cutoff-frequencies [8, 11] Hz.
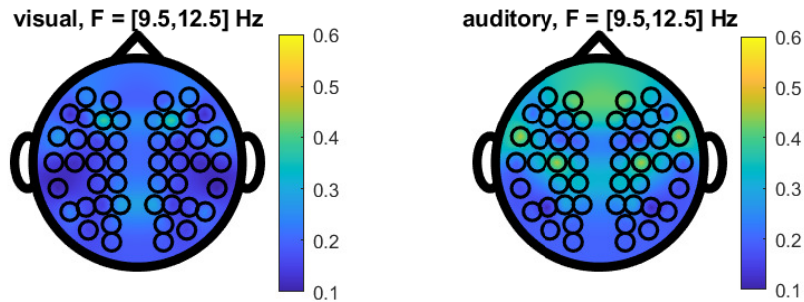
(b) PLI was calculated for filtered signals with cutoff-frequencies [9.5, 12.5] Hz.
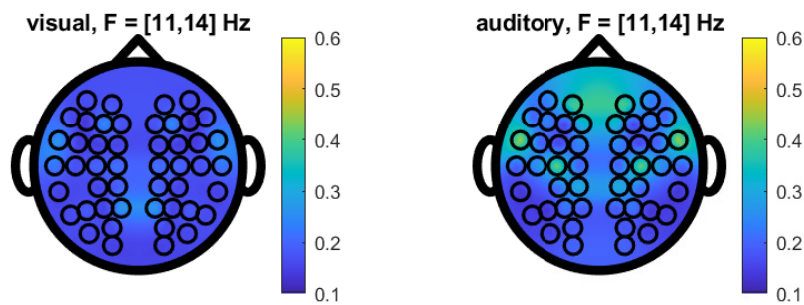
(c) PLI was calculated for filtered signals with cutoff-frequencies [11, 14] Hz.

Figure 5.5: A selection of topographical maps of the PLI between opposite channels. In the left plots PLI was calculated for signals between 0 and 0.6 s, and in the right plots between 0.6 and 2.0 s.
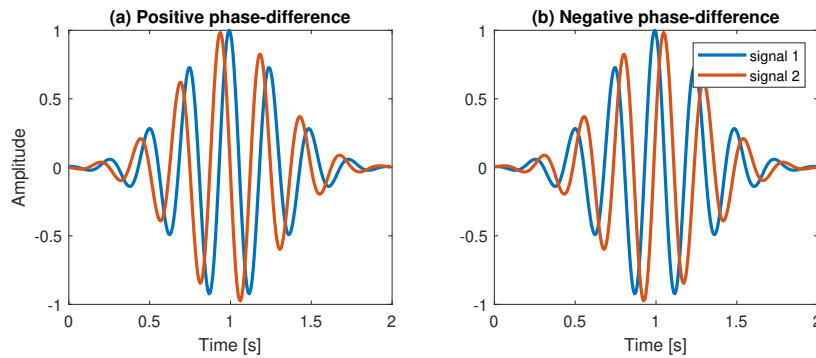

Figure 5.6: Plots of signal pairs with different phase. In (a) $\Delta\phi > 0$ and in (b) $\Delta\phi < 0$. In (a), signal 2 "comes before" signal 1, and vice versa in (b).

5.2.3   Results

In Table 5.3, the proportion correctly classified trials are listed, as well as the corresponding p-value for a binomial distribution with $n = 352$ trials and probability $p = 0.5$. If the classifications are random, it should be equally likely for the trial to be classified as "left", that is when $\hat{k} = \{-9, -8, ..., -1\}$, or right, when $\hat{k} = \{1, 2, ..., 9\}$. In the column called "total" the total proportion correct classifications are listed. In "left" and "right" the proportion correct classifications from respective sound-side are listed. In 174 trials, the word was presented in the left ear and in the remaining 178 trials, the word was presented in the right ear.

Table 5.3: In the first column, the channel pairs are listed. To the right, in column two and three, is the proportion correctly classified trials when the true sound side was either left or right. The total proportion correct classifications are listed in column four. The corresponding p-value for a binomial distribution with probability $p = 0.5$, is shown in the last column.

Channel-pair	left	right	total	p-value
TF7-TF8	0.6092	0.5393	0.5739	0.0023
C3-C4	0.6034	0.5225	0.5625	0.0082
AF3-AF4	0.5460	0.6067	0.5767	0.0017

For all channel-pairs, around 57% of the trials were correctly classified. Although these stats aren't very good for a usable classifier, it could be an indication that the algorithm does find some signals which have different relative phases depending on the presented sound side.

Another less exciting explanation could be that the algorithm classified noise present in all channels due to source leakage. Then, the algorithm was calibrated to make the noise seem like a reasonable classifier, which was also found in the other channels.

To further investigate the validity of these findings, it would be interesting to test the algorithm on other subjects in the study, using the same parameters. It would also be interesting to test the algorithm on a simpler data set without visual stimulation and with simpler auditory stimulation.

The signal scaling parameters were on average estimated to 35, which is the same as the initial window scaling parameter. At the time of writing, it is unknown whether this is a coincident or not.

6   Conclusions

6.1   Which TF-concentration measurement is best suited for evaluation?

From the initial simulations, we found that the RE and the TFC displayed similar performance in both parts of the two-step algorithm. The measurements were almost identical for the white noise simulations, except that the TFC gave a higher number of correct estimations estimations when the signal scaling parameter was underestimated. During the EEG noise simulations it moreover appeared to be less sensitive to source leakage, but generally resulted in more random estimations which gave slightly larger MSE. This is reasonable as the other measurements instead estimated the source leakage zero-lag. Although the RE was ultimately used, the TFC could possibly be a more suitable option.

6.2   How accurate is the two-step algorithm in comparison to other methods?

The two-step algorithm showed superior performance when disturbance signals close in frequency was present. This is of course reasonable as the other methods were limited to the time-domain, and unable to separate signals in frequency. In this sense, it is possible that the two-step algorithm had an unfair advantage, as the signals are represented in TF-domain.

The algorithm was more sensitive to disturbances close in time than the Hilbert transform and Pearson's linear correlation coefficient. To what extent this is something inherent to the method, and how it is affected by the chosen evaluation window should be further investigated.

The two-step algorithm resulted in more accurate estimations when the SNR was low and any disturbance was adequately far away from the signal of interest. In high SNR, the other methods were more accurate. As the resulting MSE of the algorithm estimations still was lower than the MSE from the Hilbert transform, it is reasonable to believe that the matched window assumption was violated in some cases, causing the estimations to deviate one or two samples. When precise estimations are required in high SNR settings, this is of course a problem. However, if the SNR is high, there may be more information available about the signal envelope, and it would perhaps be unnecessary to estimate the signal scaling parameter.

The method furthermore assumes the signals to be Gaussian, which isn't always applicable.

6.3 Is it possible to estimate phase-lag between EEG-signals using the two-step algorithm?

From the flickering light example, we saw that the algorithm indeed could estimate the phase-lag with reasonable results. However, the practicality of the method is worth discussing.

First of all, the method is very slow compared to for example the Hilbert transform. The algorithm is thus ill-suited for exploratory purposes. Furthermore, the algorithm requires some prior information about the signals of interest, such as its location in time and frequency, and preferably also a suitable signal scaling parameter. Only then can the initial parameters be set efficiently.

In EEG, the Hilbert transform is mainly used in phase-synchronization measurements such as PLI and PLV. Whether the two-step method or the MPR could be used for similar purposes could be further investigated.

All concentration measurements in the MPR in the two-step algorithm were affected by source leakage and became more or less biased towards zero-lag. This could possibly be reduced if the algorithm was combined with a spatial filter to remove spurious connectivity, such as the surface Laplacian.

Bibliography

[1]   Leif Sörnmo and Pablo Laguna. *Bioelectrical signal processing in cardiac and neurological applications*. Vol. 8. Academic Press, 2005.

[2]   ZT Al-Qaysi, BB Zaidan, AA Zaidan and MS Suzani. 'A review of disability EEG based wheelchair control system: Coherent taxonomy, open challenges and recommendations'. In: *Computer methods and programs in biomedicine* 164 (2018), pp. 221–237.

[3]   Björn Kralemann, Arkady Pikovsky and Michael Rosenblum. 'Reconstructing effective phase connectivity of oscillator networks from observations'. In: *New Journal of Physics* 16.8 (2014), p. 085013.

[4]   Juergen Fell and Nikolai Axmacher. 'The role of phase synchronization in memory processes'. In: *Nature reviews neuroscience* 12.2 (2011), pp. 105–118.

[5]   Maria Sandsten, Rachele Anderson, Isabella Reinhold and Johan Brynolfsson. 'The matched reassigned cross-spectrogram for phase estimation'. In: *ICASSP 2020-2020 IEEE International Conference on Acoustics, Speech and Signal Processing (ICASSP)*. Barcelona, Spain, 2020, pp. 5960–5964.

[6]   Maria Sandsten and Johan Brynolfsson. 'The scaled reassigned spectrogram with perfect localization for estimation of Gaussian functions'. In: *IEEE Signal Processing Letters* 1 (2015), pp. 100–104.

[7]   Johan Brynolfsson and Maria Sandsten. 'Parameter estimation of Oscillating Gaussian functions using the scaled reassigned spectrogram'. In: *Signal Processing* 150 (2017), pp. 20–32.

[8]   Maria Sandsten. 'Time-frequency analysis of time-varying signals and non-stationary processes'. In: *Lund University* (2016).

[9]   Kunihiko Kodera, Claude De Villedary and Roger Gendrin. 'A new method for the numerical analysis of non-stationary signals'. In: *Physics of the Earth and Planetary Interiors* 12.2-3 (1976), pp. 142–150.

[10] Maria Sandsten, Johan Brynolfsson and Isabella Reinhold. 'The matched window reassignment'. In: *2018 26th European Signal Processing Conference (EU-SIPCO)*. Rome, Italy, 2018, pp. 2340–2344.

[11] Maria Sandsten, Isabella Reinhold and Josefin Starkhammar. 'Automatic time-frequency analysis of echolocation signals using the matched Gaussian multitaper spectrogram'. In: *INTERSPEECH* (2017), pp. 3048–3052.

[12] Tzu-Hsien Sang and William J Williams. 'Renyi information and signal-dependent optimal kernel design'. In: *1995 International Conference on Acoustics, Speech, and Signal Processing*. Vol. 2. IEEE. 1995, pp. 997–1000.

[13] Niall Hurley and Scott Rickard. 'Comparing measures of sparsity'. In: *IEEE Transactions on Information Theory* 55.10 (2009), pp. 4723–4741.

[14] Simon Hanslmayr and Tobias Staudigl. 'How brain oscillations form memories—a processing based perspective on oscillatory subsequent memory effects'. In: *Neuroimage* 85 (2014), pp. 648–655.

[15] Elham Barzegaran, Sebastian Bosse, Peter J Kohler and Anthony M Norcia. 'EEGSourceSim: A framework for realistic simulation of EEG scalp data using MRI-based forward models and biologically plausible signals and noise'. In: *Journal of neuroscience methods* 328 (2019), p. 108377.

[16] Blausen Medical. 'Medical gallery of blausen medical 2014'. In: *WikiJournal of Medicine* 1.2 (2014), pp. 1–79.

[17] Brylie Christopher Oxley. *International 10-20 system for EEG-MCN*. URL: https://commons.wikimedia.org/wiki/File:International_10-20_system_for_EEG-MCN.svg. (accessed: 27.08.2021).

[18] Bin He, Laura Astolfi, Pedro Antonio Valdés-Sosa, Daniele Marinazzo, Satu O Palva, Christian-George Bénar, Christoph M Michel and Thomas Koenig. 'Electrophysiological brain connectivity: theory and implementation'. In: *IEEE Transactions on Biomedical Engineering* 66.7 (2019), pp. 2115–2137.

[19] Sergul Aydore, Dimitrios Pantazis and Richard M Leahy. 'A note on the phase locking value and its properties'. In: *Neuroimage* 74 (2013), pp. 231–244.

[20] Susan M Bowyer. 'Coherence a measure of the brain networks: past and present'. In: *Neuropsychiatric Electrophysiology* 2.1 (2016), pp. 1–12.

[21] Christopher K Kovach. 'A biased look at phase locking: Brief critical review and proposed remedy'. In: *IEEE Transactions on signal processing* 65.17 (2017), pp. 4468–4480.

[22] Rosaleena Mohanty, William A Sethares, Veena A Nair and Vivek Prabhakaran. 'Rethinking measures of functional connectivity via feature extraction'. In: *Scientific reports* 10.1 (2020), pp. 1–17.

[23] Michael X Cohen. 'Effects of time lag and frequency matching on phase-based connectivity'. In: *Journal of neuroscience methods* 250 (2015), pp. 137–146.

[24] Louis Litwin. 'FIR and IIR digital filters'. In: *IEEE potentials* 19.4 (2000), pp. 28–31.

[25] Fredrik Gustafsson. 'Determining the initial states in forward-backward filtering'. In: *IEEE Transactions on signal processing* 44.4 (1996), pp. 988–992.

[26] Sandra Persson. 'An ERP Study of Competitive Memory Retrieval in a Lateralized Auditory Task'. MA thesis. Lund University, 2019.

A Appendix

A.1 Derivation of Matched Phase Reassignment variant

In the beginning of the thesis, a combination of the MPR and ScRe-Spec was used to estimate (σ, k) in a grid of candidates. A short derivation of this method is presented here.

Assume two signals described by

$$y_n(t) = A_n x(t) e^{-i\phi_n} \tag{A.1}$$

where A_n is the amplitude and ϕ_n is the phase and x is a transient signal given by

$$x(t) = a(t - t_0) e^{-i\omega_0 t} \tag{A.2}$$

where t_o, f_0 are the centre time and frequency, and a describes the signal envelope. The cross-spectrogram between two such signals is as usual given by

$$S_{y_1,y_2}^h(t, \omega) = F_{y_1}^h(t, \omega)(F_{y_1}^h(t, \omega))^*, \tag{A.3}$$

where $F_{y_n}^h$ is the STFT with some window function h. In Sandsten et al. [5], the general reassigned cross-spectrogram is given by

$$RS_{y_1,y_2}^h(t, \omega) = \int \int |S_{y_1,y_2}^h(s, \xi)| \delta(t - \hat{t}_{y_1,y_2}(s, \xi)) \delta(\omega - \hat{\omega}_{y_1,y_2}(s, \xi)) \mathrm{d}s \mathrm{d}\xi, \tag{A.4}$$

with the following reassignment vectors

$$\hat{t}_{y_1,y_2}(t, \omega) = t + c_t \Re \left(\frac{F_{y_1}^{th}(t, \omega)}{F_{y_2}^h(t, \omega)} + \frac{F_{y_2}^{th}(t, \omega)}{F_{y_1}^h(t, \omega)} \right) \tag{A.5}$$

$$\hat{\omega}_{y_1,y_2}(t, \omega) = \omega - c_\omega \Im \left(\frac{F_{y_1}^{dh/dt}(t, \omega)}{F_{y_2}^h(t, \omega)} + \frac{F_{y_2}^{dh/dt}(t, \omega)}{F_{y_1}^h(t, \omega)} \right), \tag{A.6}$$

where

$$F_{y_n}^h(t, \omega) = A_n e^{-i\phi_n} F_x^h(t, \omega) \tag{A.7}$$

$$F_{y_n}^{th}(t, \omega) = A_n e^{-i\phi_n} F_x^{th}(t, \omega) \tag{A.8}$$

$$F_{y_n}^{dh/dt}(t, \omega) = A_n e^{-i\phi_n} F_x^{dh/dt}(t, \omega). \tag{A.9}$$

In Brynolfsson and Sandsten [7] explicit expressions of the STFT are derived. Assuming x is given by an oscillating Gaussian transient such that

$$x(t) = g_k(t) = e^{-\frac{(t - t_k)^2}{2\sigma_k^2}} e^{-j\omega_k t}, \tag{A.10}$$

and the window function in the STFT is set to $h(t) = e^{-t^2/2\lambda^2} \frac{1}{\pi^{-1/4}\sqrt{\lambda}}$, the STFT are given by

$$F_x^h(t,\omega) = \sqrt{\frac{2\lambda\sigma_k^2\sqrt{\pi}}{\lambda^2 + \sigma_k^2}} e^{-\frac{1}{2}\left(\frac{1}{\lambda^2+\sigma_k^2}(t-t_k)^2 + \frac{\lambda^2\sigma_k^2}{\lambda^2+\sigma_k^2}(\omega-\omega_k)^2\right)} e^{-i\frac{(\omega-\omega_k)(\sigma_k^2 t + \lambda^2 t_k)}{\lambda^2+\sigma_k^2}} \tag{A.11}$$

$$F_x^{th}(t,\omega) = -\frac{\lambda^2}{\lambda^2 + \sigma_k^2}(t - t_k + i\sigma_k^2(\omega - \omega_k))F_x^h(t,\omega) \tag{A.12}$$

$$F_x^{dh/dt}(t,\omega) = -\frac{1}{\lambda^2}F_x^{th}(t,\omega). \tag{A.13}$$

Inserted into Equation A.5 and A.6, the reassignment vectors can be simplified to

$$\hat{t}(t,\omega) = t - c_t \frac{A_1^2 + A_2^2}{A_1 A_2} \frac{\lambda^2}{\lambda^2 + \sigma_k^2} \cos(\phi_2 - \phi_1)(t - t_k) = t - c_t K(t - t_k) \tag{A.14}$$

$$\hat{\omega}(t,\omega) = \omega - c_\omega \frac{A_1^2 + A_2^2}{A_1 A_2} \frac{\sigma_k^2}{\lambda^2 + \sigma_k^2} \cos(\phi_2 - \phi_1)(\omega - \omega_k) = \omega - c_\omega L(\omega - \omega_k). \tag{A.15}$$

When $\Delta\phi = (\phi_2 - \phi_1) = 0$, $c_t = \frac{A_1 A_2}{A_1^2 + A_2^2} \frac{\lambda^2 + \sigma_k^2}{\lambda^2}$ and $c_\omega = \frac{A_1 A_2}{A_1^2 + A_2^2} \frac{\lambda^2 + \sigma_k^2}{\sigma_k^2}$ optimal reassignment is achieved. This is simply a combination of the reassignment vectors derived in Sandsten et al. [5] and Brynolfsson and Sandsten [7].

The idea was to estimate the signal scaling parameters and relative phase from a grid of candidates $(\sigma_{k,i}, k_i)$. For each candidate scaling parameter, the STFT would be calculated. Then, the reassigned cross-spectrogram using the new reassignment-vectors would be calculated for each candidate lag k_i and evaluated using some concentration measurement.

Calculating the RE of the MPR variant

To simplify calculations, the constants in the reassignment vectors were collected in K and L in Equation A.14 and $A.15$. All the following expressions are mostly variants of the calculations in Brynolfsson and Sandsten [7].

Inserting the STFT expression in A.7 into the absolute value of the cross-spectrogram in A.3, it is simplified to

$$|S_{y_1,y_2}^h(t,\omega)| = |F_{y_1}^h(t,\omega)(F_{y_2}^h(t,\omega))^*| = A_1 A_2|e^{i(\phi_2-\phi_1)}F_x^h(t,\omega)(F_x^h(t,\omega))^*| = A_1 A_2 S_x^h(t,\omega)$$

Inserting this, and the reassignment vectors in Equation A.14 and $A.15$ into Equation

46

A.4, the reassigned cross-spectrogram can be further expressed as

$$RS^h_{y_1,y_2}(t,\omega) = A_1 A_2 \int\int S^h_x(\tau,\xi)\delta(t-\tau+c_tK(\tau-t_k))\delta(\omega-\xi+c_\omega L(\xi-\omega_k))\mathrm{d}\tau\mathrm{d}\xi$$

$$= A_1 A_2 \int\int S^h_x(\tau,\xi)\frac{\delta(\tau-\frac{t-c_tKt_k}{1-c_tK})}{|1-c_tK|}\frac{\delta(\xi-\frac{\omega+c_\omega L\omega_k}{1-c_\omega L})}{|1-c_\omega L|}\mathrm{d}\tau\mathrm{d}\xi$$

$$= A_1 A_2 \frac{S^h_x(\frac{t-c_tKt_k}{1-c_tK},\frac{\omega+c_\omega L\omega_k}{1-c_\omega L})}{|1-c_tK||1-c_\omega L|}$$

$$= \frac{A_1 A_2 \sigma_k \lambda\sqrt{\pi}}{(\lambda^2+\sigma_k^2)|1-c_tK||1-c_\omega L|}e^{-\left(\frac{1}{\lambda^2+\sigma_k^2}(\frac{t-c_tKt_k}{1-c_tK}-t_k)^2+\frac{\lambda^2\sigma_k^2}{\lambda^2+\sigma_k^2}(\frac{\omega+c_\omega L\omega_k}{1-c_\omega L}-\omega_k)^2\right)}$$

$$= \frac{A_1 A_2 \sigma_k \lambda\sqrt{\pi}}{(\lambda^2+\sigma_k^2)|1-c_tK||1-c_\omega L|}e^{-\left(\frac{(t-t_k)^2}{(\lambda^2+\sigma_k^2)(1-c_tK)^2}+\frac{\lambda^2\sigma_k^2(\omega-\omega_k)^2}{(\lambda^2+\sigma_k^2)(1-c_\omega L)^2}\right)}.$$

The aim was then to insert this into the Rényi entropy given by

$$RE = \frac{1}{1-\alpha}\log_2\int\int\left(\frac{S(t,\omega)}{\int\int S(t,\omega)\mathrm{d}t\mathrm{d}\omega}\right)^\alpha \mathrm{d}t\mathrm{d}\omega, \qquad (A.16)$$

where $\alpha = 3$. Starting with the integral we get

$$\int\int\left(\frac{RS^h_{y_1,y_2}(t,\omega)}{\int\int RS^h_{y_1,y_2}(t,\omega)\mathrm{d}t\mathrm{d}\omega}\right)^3 \mathrm{d}t\mathrm{d}\omega =$$

$$= \int\int\left(\frac{e^{-\left(\frac{(t-t_k)^2}{(\lambda^2+\sigma_k^2)(1-c_tK)^2}+\frac{\lambda^2\sigma_k^2(\omega-\omega_k)^2}{(\lambda^2+\sigma_k^2)(1-c_\omega L)^2}\right)}}{\int\int e^{-\left(\frac{(t-t_k)^2}{(\lambda^2+\sigma_k^2)(1-c_tK)^2}+\frac{\lambda^2\sigma_k^2(\omega-\omega_k)^2}{(\lambda^2+\sigma_k^2)(1-c_\omega L)^2}\right)}\mathrm{d}t\mathrm{d}\omega}\right)^3 \mathrm{d}t\mathrm{d}\omega.$$

Denoting the constants in the exponentials as $A_t = 1/((\lambda^2+\sigma_k^2)(1-c_tK)^2)$ and $A_\omega = \lambda^2\sigma_k^2/((\lambda^2+\sigma_k^2)(1-c_\omega L)^2)$, the nominator is simply calculated to

$$\int\int e^{-A_t(t-t_k)^2-A_\omega(\omega-\omega_k)^2}\mathrm{d}t\mathrm{d}\omega = \int e^{-A_t(t-t_k)^2}\mathrm{d}t\int e^{-A_\omega(\omega-\omega_k)^2}\mathrm{d}\omega$$

$$= \sqrt{\frac{\pi}{A_t}}\sqrt{\frac{\pi}{A_\omega}}$$

$$= \frac{\pi(\lambda^2+\sigma_k^2)|1-c_tK||1-c_\omega L|}{\lambda\sigma_k}.$$

This is constant and can be moved outside the integrals. Similarly

$$\int\int\left(e^{-A_t(t-t_k)^2-A_\omega(\omega-\omega_k)^2}\right)^3 \mathrm{d}t\mathrm{d}\omega = \int e^{-3A_t(t-t_k)^2}\mathrm{d}t\int e^{-3A_\omega(\omega-\omega_k)^2}\mathrm{d}\omega$$

$$= \sqrt{\frac{\pi}{3A_t}}\sqrt{\frac{\pi}{3A_\omega}}$$

$$= \frac{\pi(\lambda^2+\sigma_k^2)|1-c_tK||1-c_\omega L|}{3\lambda\sigma_k}.$$

Then,

$$\int\int\left(\frac{RS^h_{y_1,y_2}(t,\omega)}{\int\int RS^h_{y_1,y_2}(t,\omega)\mathrm{d}t\mathrm{d}\omega}\right)^3\mathrm{d}t\mathrm{d}\omega =$$

$$= \frac{\lambda^3\sigma_k^3}{\pi^3(\lambda^2+\sigma_k^2)^3|1-c_tK|^3|1-c_\omega L|^3} \cdot \frac{\pi(\lambda^2+\sigma_k^2)|1-c_tK||1-c_\omega L|}{3\lambda\sigma_k} =$$

$$= \frac{\lambda^2\sigma_k^2}{3\pi^2(\lambda^2+\sigma_k^2)^2|1-c_tK|^2|1-c_\omega L|^2},$$

and

$$RE = -\frac{1}{2}\log_2\left(\frac{\lambda^2\sigma_k^2}{3\pi^2(\lambda^2+\sigma_k^2)^2|1-c_tK|^2|1-c_\omega L|^2}\right) =$$

$$= \log_2\left(\sqrt{3}\pi(\lambda^2+\sigma_k^2)|1-c_t\frac{A_1^2+A_2^2}{A_1A_2}\frac{\lambda^2}{\lambda^2+\sigma_k^2}\cos(\phi_2-\phi_1)|\right.$$

$$\left.|1-c_\omega\frac{A_1^2+A_2^2}{A_1A_2}\frac{\sigma_k^2}{\lambda^2+\sigma_k^2}\cos(\phi_2-\phi_1)|\right) - \log_2(\lambda\sigma_k),$$

where L and K was expressed fully.

A.2 Estimation of time-lag k with no added noise

In Section 4.3, the MPR was used to estimate time-lag. When the matched window assumption was violated, the number of exactly correct estimations decreased. This can be seen also when no noise is added.
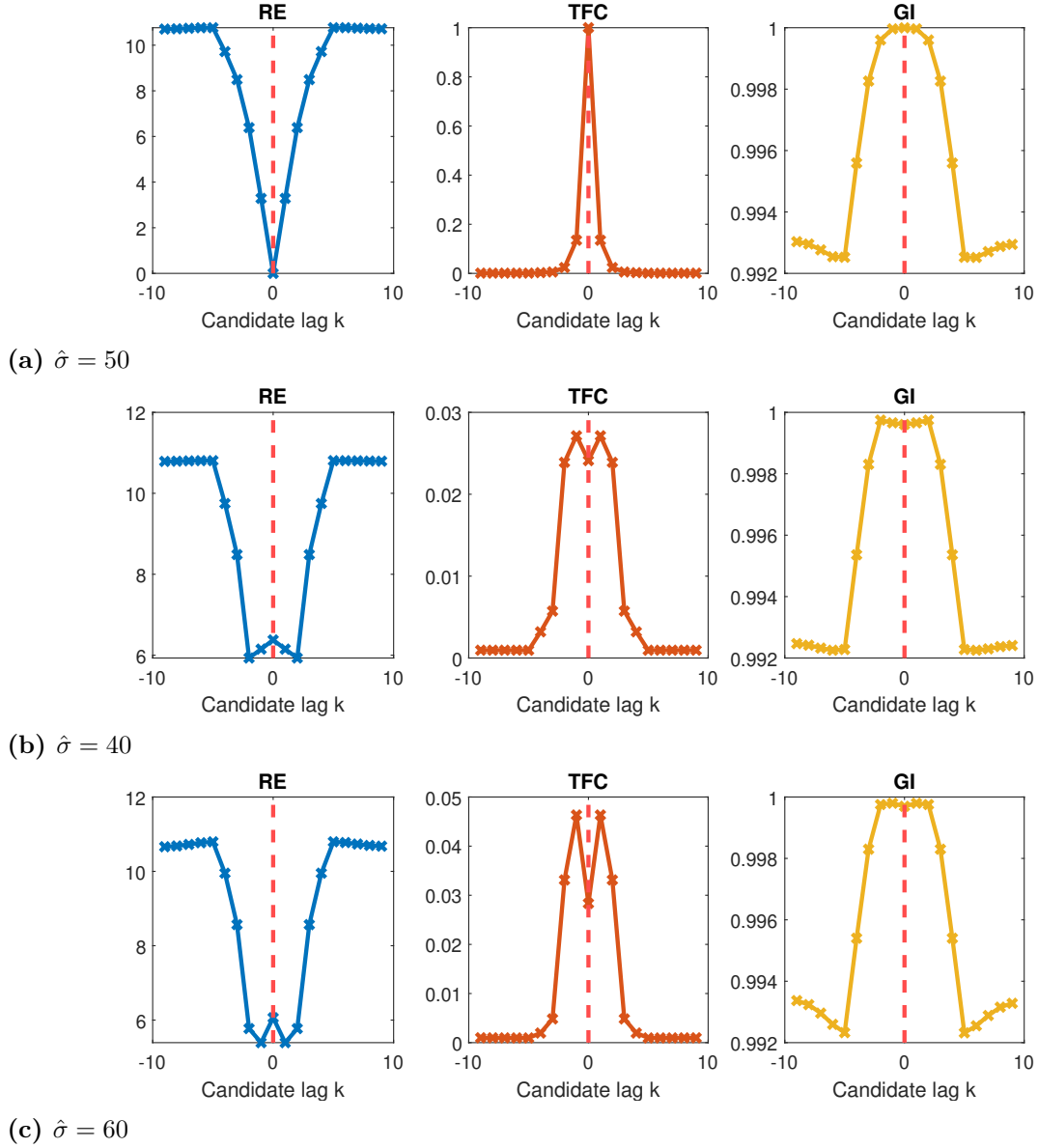

(a) $\hat{\sigma} = 50$

(b) $\hat{\sigma} = 40$

(c) $\hat{\sigma} = 60$

Figure A.1: Resulting concentration measurements of MPR with different applied time-lags k. The true phase-difference is zero, and thus the true time-lag is $k_0 = 0$, which is marked with a red dashed line. In (a), (b) and (c), different window functions $\hat{\sigma}$ in the STFT in the MPR are used.

I Figure A.1a to A.1c, the considered concentration measurements are evaluated over MPR for different time-lags k. The signals were simulated as in Section 4.3, with $\sigma = 50$ but with no added noise and the relative phase was set to zero, which corresponds to zero time-lag. When the window is matched as in (a), $\lambda = \hat{\sigma} = \sigma$, all concentration measurements find the correct time-lag. However, when the matched window assumption is violated, as in (b) and (c), $\lambda = \hat{\sigma} \neq \sigma$, a small peak or valley

appears for the correct time-lag.

In Figure A.2, two MPR are plotted with window scaling parameters $\hat{\sigma} = 60$, but with different time-shifts k. In (b), the MPR is made when one signal has been shifted $k = 0$ samples, which is the true phase-lag that we aim to estimate. In (a) however, the MPR is made with time-shift $\hat{k}$, which is the lag that minimised the RE. Through visual assessment of the MPRs, we see that the RE made a reasonable estimation as the MPR with $k = 1$ looks more concentrated. Thus the estimation errors are not the fault of the concentration measurements, but the fault of the reassignment when the matched window assumption isn't fulfilled.
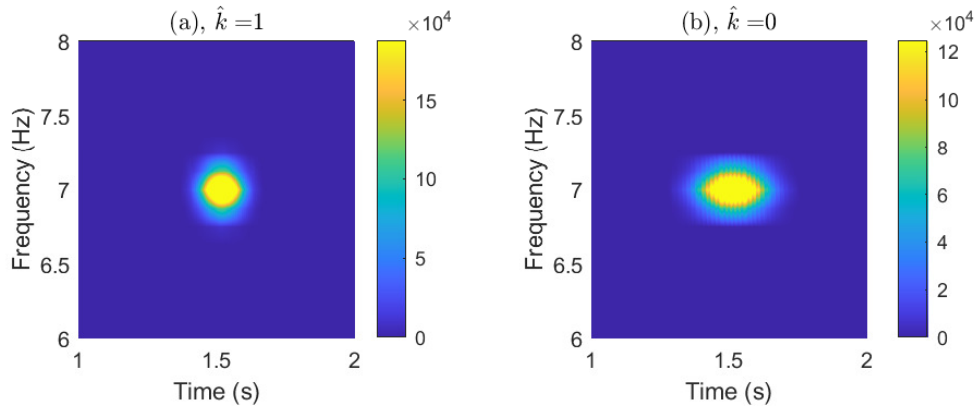

Figure A.2: MPR with $\hat{\sigma} = 60$ (True scaling parameter is $\sigma = 50$) but different time-shifts k.

A.3   Amplitude estimation

When testing the ScRe-Spec and MPR through simulations, the amplitudes were both one and assumed to be known. In this simulation, the entire and final two-step algorithm was used to estimate the time-lag k between two signals with different amplitudes. The amplitudes were set to $A_1 = 1$ and $A_2 = 0.5$. Phase and relative phase were generated as $\phi_1 \sim \mathcal{U}(-\pi, \pi)$ and $\Delta\phi \sim \mathcal{U}(-7\pi/8, 7\pi/8)$.

In Figure A.3, the estimation results using white noise can be seen. The same plots but using EEG noise in the simulations are seen in Figure A.4. From the white noise plot, we see that the algorithm which estimates amplitude from the spectrogram show superior performance. From the EEG simulations, the amplitude estimations from the spectrogram and time-series perform equal.

As the amplitude estimates from the spectrogram were better or as good as the estimations from the time representation, it was chosen as the estimation method of choice in the two-step algorithm.
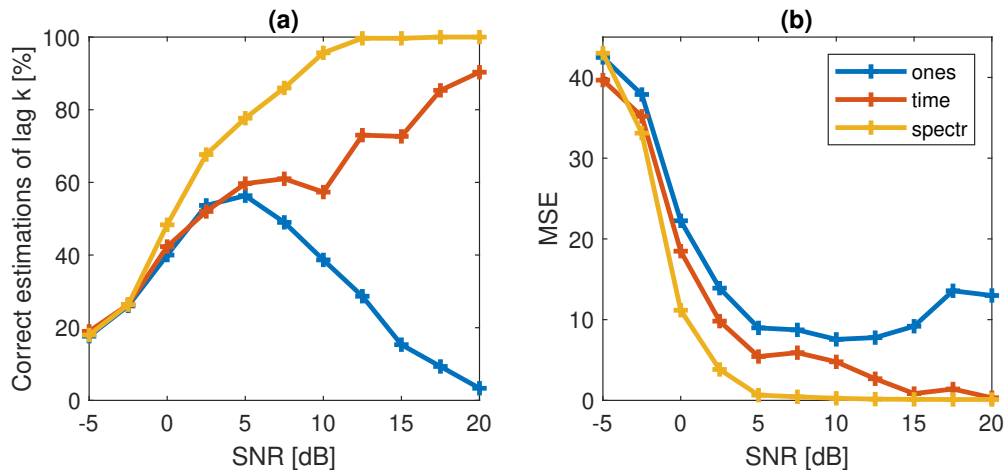

Figure A.3: Estimation of time-lag k using 2-step algorithm with the RE. The signals were simulated using white noise, and $A_1 = 1$ and $A_2 = 0.5$. In the algorithm the signals are estimated as ones, as the maximum amplitude in time or as the square root of the maximum amplitude in the spectrogram.
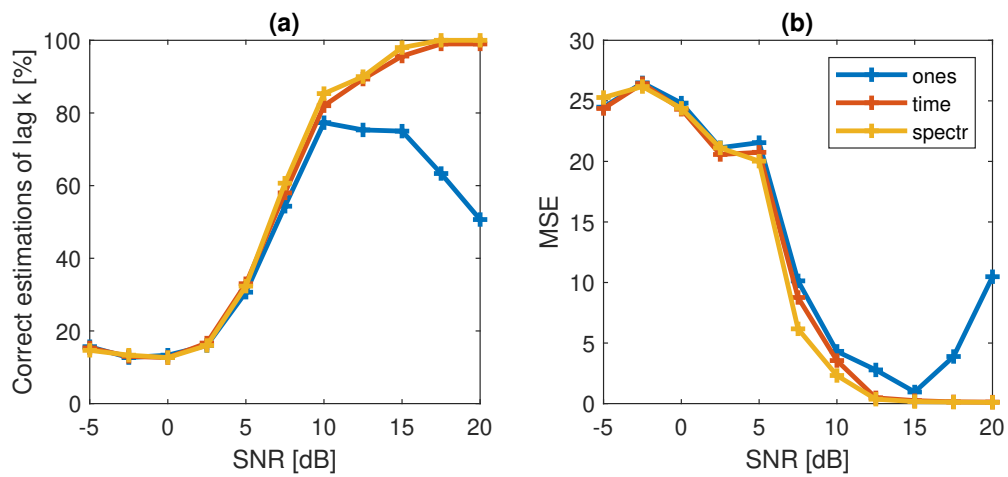
Figure A.4: Estimation of time-lag k using 2-step algorithm with the RE. The signals were simulated using EEG noise, and $A_1 = 1$ and $A_2 = 0.5$. In the algorithm the signals are estimated as ones, as the maximum amplitude in time or as the square root of the maximum amplitude in the spectrogram.